

## Dual-Doppler and Single-Doppler Analysis of a Tornadic Storm Undergoing Mergers and Repeated Tornadogenesis

JOSHUA WURMAN

*Center for Severe Weather Research, Boulder, Colorado*

YVETTE RICHARDSON

*The Pennsylvania State University, University Park, Pennsylvania*

CURTIS ALEXANDER

*School of Meteorology, University of Oklahoma, Norman, Oklahoma*

STEPHEN WEYGANDT

*National Oceanic and Atmospheric Administration/Earth System Research Laboratory, Boulder, Colorado*

PENG FEI ZHANG

*Cooperative Institute for Mesoscale Meteorological Studies, University of Oklahoma, Norman, Oklahoma*

(Manuscript received 3 January 2006, in final form 6 April 2006)

### ABSTRACT

Dual-Doppler observations with unprecedented finescale spatial and temporal resolution are used to characterize the vector wind field in and near a tornado occurring near Kiefer, Oklahoma, on 26 May 1997. Analyses of the dual-Doppler vector wind fields document in detail, for the first time, several structures associated with the tornado: a proximate updraft region, a rear-flank downdraft wrapping around the tornado, a double gust front structure occluding near the tornado, and a region of enhanced vorticity separated from the tornado that may have been associated with cyclic tornadogenesis. The analyses are compared to conceptual and computer models of tornadic storms.

A subsequent tornadogenesis was observed with radar every 18 s, providing a finescale temporal view of the genesis process. The genesis process was complex and the evolution of tornado intensity parameters was not monotonic in time. Low-level rotation contracted and intensified, then broadened, then contracted and intensified a second time to form the tornado.

The initial tornadogenesis was coincident with the merger of the main supercell and a much smaller convective storm. This tornado, which was always surrounded by substantial precipitation originating from both storms, began to dissipate just a few minutes after genesis, and the rotation both aloft and near the surface weakened substantially. A second storm merger, with a much larger and supercellular storm, was coincident with a reintensification of the mesocyclone aloft, a new hook echo development, and the genesis of a short-lived tornado. After the dissipation of this second tornado, the merger disrupted the structure of the supercell storm, the hook echo was absorbed, and the mesocyclone dissipated. The current analysis suggests a process in which storm mergers may, in sequence, aid tornadogenesis by enhancing surface convergence, or through another mechanism, but subsequently disrupt the tornado's parent supercell perhaps by cooling the inflow air, with the result being short-lived tornadoes.

### 1. Introduction

Tornadic storms, and tornadogenesis in supercellular storms have been observed visually, with surface obser-

—  
vations, and with radars for decades (e.g., Stout and Huff 1953; Ludlam 1963; Fujita 1975; Ray et al. 1975, 1981; Brandes 1977, 1978, 1981, 1984a; Fujita and Wakimoto 1982; Brandes et al. 1988; Dowell and Bluestein 1997, 2002a,b; Wakimoto and Liu 1998; Trapp 1999; Trapp et al. 1999; Wakimoto and Cai 2000; Bluestein and Gaddy 2001; Klemp et al. 1981; Lemon

*Corresponding author address:* Joshua Wurman, Center for Severe Weather Research, 1945 Vassar Circle, Boulder, CO 80305.  
E-mail: jwurman@cswr.org

DOI: 10.1175/MWR3276.1

and Doswell 1979; Rasmussen et al. 1982; Jensen et al. 1983; Markowski et al. 2002). In some of these studies, dual-Doppler observations have permitted vector wind fields to be synthesized and dynamically important derived quantities such as divergence and vorticity to be calculated. While these studies have been useful in probing the structure and mechanisms of tornadogenesis, maintenance, and other issues, they have either been single Doppler or have been limited by the resolution of the measurements. Radar beam spreading and coarse range sampling have resulted in typical data spacings of 500 to 1000 m and resolution volumes of  $10^8$ – $10^9$  m<sup>3</sup>. As a result, significant features in the lowest 1 km of the storms, including strong divergence in the rear-flank downdraft, convergence in the updraft, and vorticity in the tornado and its surroundings have not been well resolved. Airborne dual-Doppler analyses (Dowell and Bluestein 2002a,b) obtained data with resolution volumes of about  $10^8$  m<sup>3</sup>, and documented, in more detail, the process of cyclic tornadogenesis in one storm. However, the resolution was still too coarse to accurately resolve details in the structures exhibiting spatial scales less than 1 km (Carbone et al. 1985). More importantly, airborne dual-Doppler calculations are problematical in the region of 0–1 km AGL, where strong ground clutter contaminates the Doppler wind fields. High-resolution observations of tornadic storms using ground-based mobile radars (Wurman et al. 1996; Wurman and Gill 2000; Wurman 2002; Bluestein and Pazmany 2000; Bluestein et al. 2003; Alexander and Wurman 2005; Wurman and Alexander 2005; Lee and Wurman 2005; Dowell et al. 2005; Tanamachi et al. 2006, Wurman et al. 2007a) reveal a great deal of fine-scale detail but only employ a single radar, and thus are unable to measure the full vector wind field. Therefore, important dynamical quantities such as convergence and vorticity have not been calculated directly.

Computational studies have simulated the evolution of tornado-like vortices and their environments (Wicker and Wilhelmson 1995; Klemp et al. 1981; Adlerman et al. 1999; Adlerman 2003; Klemp and Rotunno 1983; Wicker et al. 2002; Romine et al. 2004; Xue 2004). These simulations reproduced structures within tornadic storms and evolutionary behavior consistent with those suggested by conceptual models, including rear-flank downdrafts wrapping around the tornadoes, single and double gust fronts, and cyclic tornadogenesis. However, many of these computational results have not, until now, been confirmed with actual high-resolution dual-Doppler radar observations.

During the previous decade, the Doppler on Wheels (DOW) radars were able to obtain several dual-

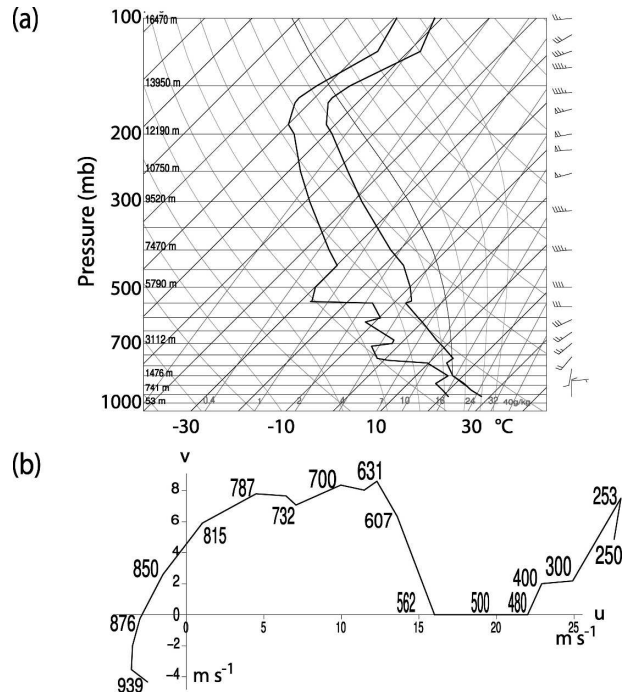


FIG. 1. Springfield, MO, sounding valid at 0000 UTC 27 May 1997 with (a) a skew  $T$ - $\log p$  diagram representing thermodynamic characteristics of the warm moist sector and (b) a hodograph depicting the kinematic characteristics of the environment.

Doppler datasets, permitting the calculation of 2D, 3D, and 4D vector wind fields in and near tornadoes. This paper presents the analyses of the first of these datasets, which was collected near Kiefer, Oklahoma, in 1997.

## 2. Synoptic and mesoscale environment

The synoptic environment on 26 May 1997 was conducive to the development of organized deep moist convection across the southern plains of the United States. Moderate deep-layer shear was present across Oklahoma at 0000 UTC on 27 May as the vertical wind profile in eastern Oklahoma contained about  $23$  m s<sup>-1</sup> of deep-layer shear (surface to 5.5 km), and about  $8$  m s<sup>-1</sup> of low-level shear (surface to 1 km). Potential instability was evident in the lifted index field with a minimum axis extending northeastward across eastern Oklahoma with values near  $-9^\circ$ .

The sounding from Springfield, Missouri (KSGF) (Fig. 1a), at 0000 UTC 27 May showed about  $2500$  J kg<sup>-1</sup> of convective available potential energy (CAPE). Soundings taken at Norman, Oklahoma (not shown), and Springfield also revealed an east–west gradient in convective inhibition (CIN), with the cap nearly re-

moved at Springfield at 0000 UTC (Colby 1984). Estimated 0–3-km storm-relative helicity of nearly  $250 \text{ m}^2 \text{ s}^{-2}$  was seen in the cyclonically curved hodograph taken from Springfield (Fig. 1b). The combination of moderate deep-layer shear and high potential instability showed the environment was supportive of the development of organized deep moist convection including supercells (Weisman and Klemp 1982; Rasmussen and Blanchard 1998).

A surface low pressure center of about 1003 mb moved east across northeastern Oklahoma between 2200 UTC 26 May and 0100 UTC 27 May (Figs. 2a,b). Associated with this low pressure center were several wind shift lines and associated pressure troughs. Temperature and moisture gradients were small across the wind shift lines, and less than that typically associated with surface fronts ( $10^\circ\text{C}$  per 100 km) or a dryline (Neiman et al. 1998; Sanders and Hoffman 2002). These boundaries likely enhanced low-level mass and moisture convergence especially across northeastern Oklahoma.

### 3. WSR-88D observations of the Kiefer–Glenpool, Oklahoma, supercell

The Weather Surveillance Radar-1988 Doppler (WSR-88D) located near Tulsa, Oklahoma (KINX), observed the initiation of several isolated thunderstorms about 110 km to the northwest of Tulsa at 2200 UTC. More thunderstorms quickly developed along wind shift lines, yielding a west–east and a north–south broken line of supercells by 2330 UTC.

KINX observed several thunderstorms oriented in a north–south broken line as they passed 10–40 km south of Tulsa during 2300–0100 UTC. At 2327 UTC one cell (hereafter referred to as storm A) near the northern end of the broken line developed a prominent hook echo in the  $0.5^\circ$  base reflectivity while containing an area of almost pure rotation in the Doppler velocity field immediately to the west of a more convergent region (Fig. 3a). Storm A was about 50 km to the southwest of KINX, near the town of Kiefer placing the elevation of the  $0.5^\circ$  scan at about 500 m AGL. The stronger area of rotation was collocated with the reflectivity hook while the more convergent region was observed along the forward flank.

A less mature, smaller, and lower reflectivity cell (hereafter referred to as storm B) approached storm A from the southwest. By 2327 UTC the cells' 15-dBZ isolines were separated by less than 5 km (Fig. 3a), and the region of convergence in storm A was positioned near the shortest distance between the 15-dBZ isolines. At 2332 UTC, the two storms collided and partially

merged with 50-dBZ isolines now within 5 km of each other (Fig. 3b). The Doppler velocity field had evolved dramatically with a single area of now significantly stronger rotation containing a Doppler velocity difference of  $49 \text{ m s}^{-1}$  and an implied axisymmetric vertical vorticity (twice the azimuthal shear of the Doppler velocity) of  $0.1 \text{ s}^{-1}$ . A single larger storm remained after the merger (hereafter referred to as storm A'; Fig. 3c). While the radar reflectivity appeared less organized with the resulting cell lacking a hook echo, the Doppler velocity field continued to display a single larger area of strong rotation.

At 2342 UTC storm A' continued to lack the radar reflectivity characteristics of an organized supercell (Fig. 3d). Furthermore, the rotation had started to weaken. By 2347 UTC, the storm A' forward-flank core was becoming more apparent with an expansion of the area with radar reflectivities over 55 dBZ and a sharper reflectivity gradient along the southern edge (Fig. 3e). The mesocyclone was considerably weaker. Another storm, which was large and exhibited mature supercellular characteristics (hereafter referred to as storm C), was approaching storm A' from the southwest with little more than a few kilometers of separation between the respective 15-dBZ isolines.

At 2352 UTC (Fig. 3f) a developing reflectivity inflow notch was visible in the southwestern portion of storm A' with a broad region of suggested convergence and weak rotation along the southern edge of the forward-flank core. By 2357 UTC storm A' was developing a new hook echo on its southwestern side while maintaining convergence along its forward-flank edge (Fig. 3g). The low-level mesocyclone remained broad and weak. In the following 300 s, the low-level mesocyclone intensified rapidly with outbound Doppler velocities of  $26 \text{ m s}^{-1}$ . Precipitation continued to wrap around the back side of the storm helping to better define the hook echo (Fig. 3h). Storm C's 15-dBZ isoline on its northern edge was located only 5 km south of the southern edge of the storm A' hook echo at this time.

At 0007 UTC storm A' again showed a classic radar presentation of a mature supercell with a well-defined hook echo and a reflectivity disk at the end of the hook (Fig. 3i). The forward-flank core had attained reflectivities over 60 dBZ with a reflectivity minimum (notch) in the downstream portion of the echo. The mesocyclone also appeared stronger, with an area of implied axisymmetric convergence (twice the measured radial shear of Doppler velocity) exceeding  $0.02 \text{ s}^{-1}$  located just to the east of the mesocyclone where the 30-dBZ isolines between the southern (northern) edge of the forward-flank of storm A' (storm C) were now in

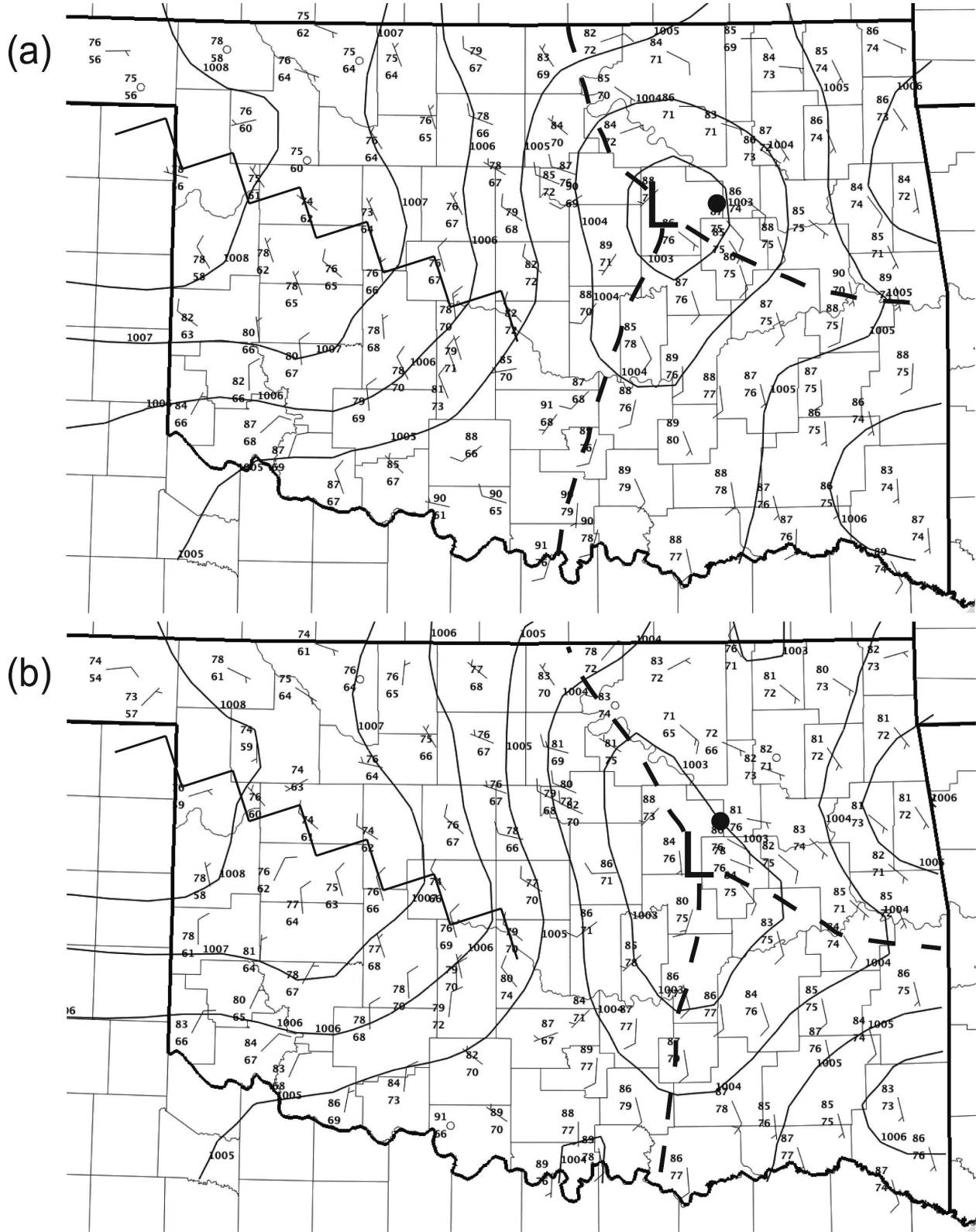


FIG. 2. Mesoscale surface analysis from the Oklahoma Mesonet showing mean sea level pressure (solid lines in mb) including troughs (dashed lines), ridges (serrated lines), and station observations of 1.5-m temperature and dewpoint ( $^{\circ}$ F), and 10-m wind vector (kt) at (a) 2300 UTC 26 May 1997 and (b) 0000 UTC 27 May 1997. The location of Kiefer, OK, is shown (circle).

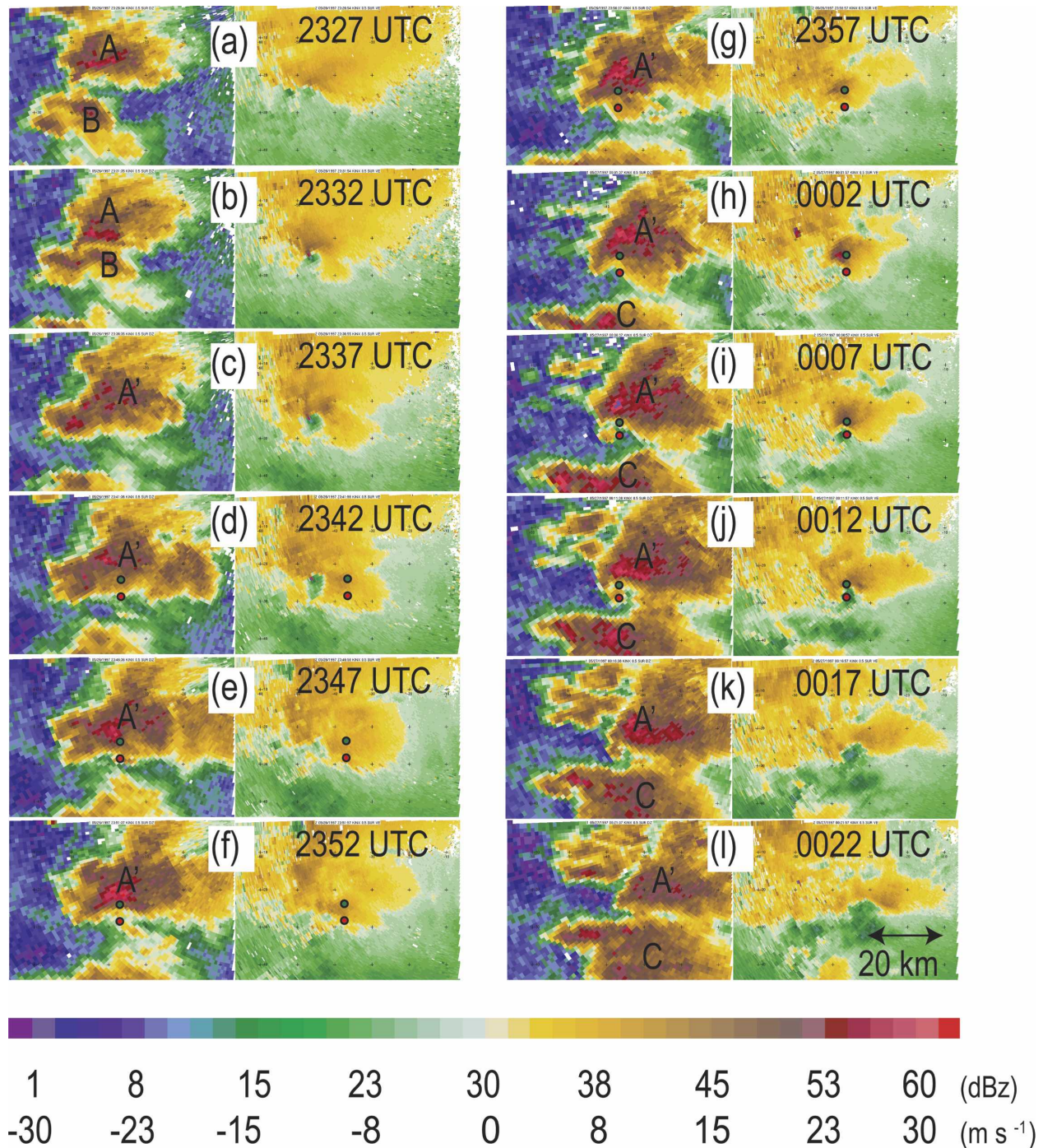


FIG. 3. The 0.5° elevation scan of convective storms A, B, A', and C from KINX (located just off the upper-right corner) showing (left) base reflectivity and (right) Doppler velocity at several times during the evolution of the tornadoes near Kiefer and Glenpool, OK. The locations of DOW2 (red circle) and DOW3 (green circle) are shown.

contact. At 0012 UTC the low-level mesocyclone in storm A' continued to intensify as the merger proceeded along the forward-flank cores (Fig. 3j). The storm A' hook echo was now almost completely sur-

rounded by radar reflectivities in excess of 30 dBZ within 2 km.

By 0017 UTC the hook echo from storm A' was not as well defined (Fig. 3k). The Doppler velocity field still

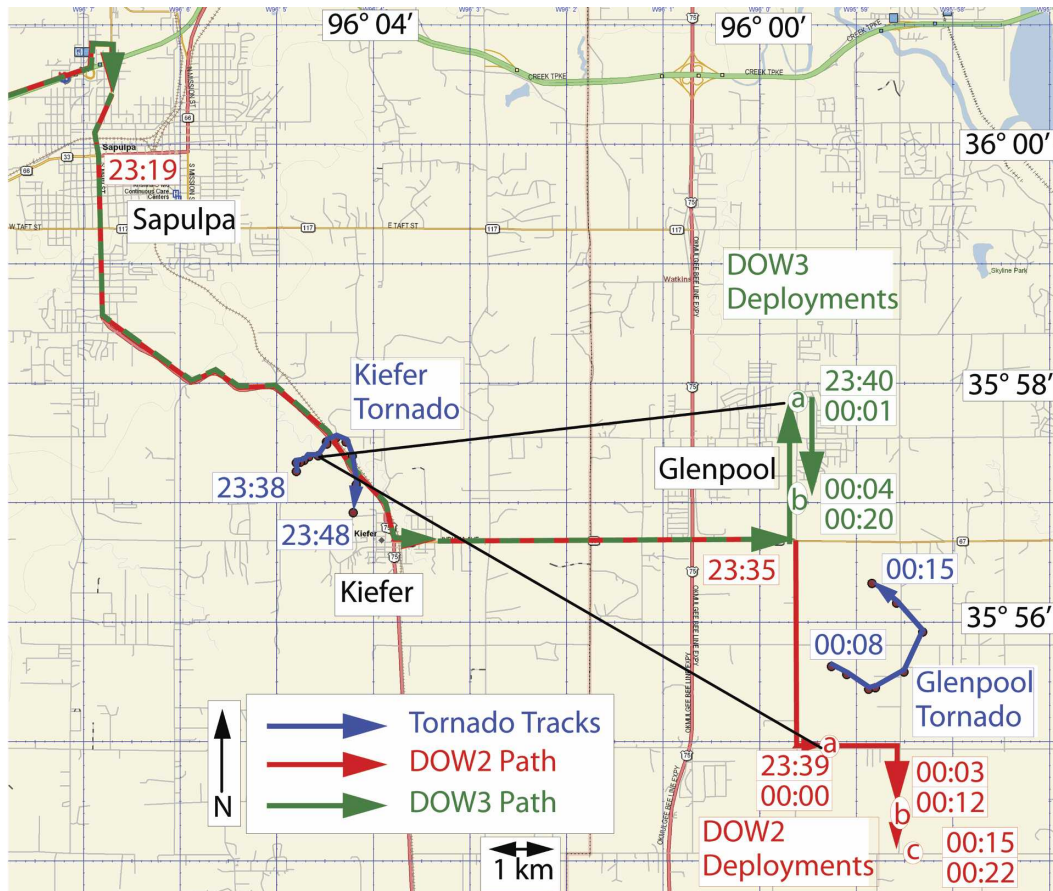


FIG. 4. Map of DOW deployments and the tracks of Kiefer and Glenpool, OK, tornadoes. (a) DOW deployment locations for Kiefer dual-Doppler study. (b) DOW observation locations and (c) during genesis of Glenpool tornado. Tornado tracks (blue) as determined by DOW observations, accurate within 50 m.

displayed a large low-level mesocyclone with the persisting convergent region a few kilometers to its east. The storm merger continued through 0022 UTC by which time the maximum reflectivity of storm A' continued to decrease and the once prominent hook echo now appeared absent (Fig. 31). The low-level mesocyclone had also started to weaken, although a broad area of rotation persisted. The northern 30-dBZ edge of storm C was now in contact with almost the entire southern flank of storm A'. In the following 600 s the storm merger continued and storm A' became ill defined.

#### 4. Mobile radar deployment, observations, and dual-Doppler synthesis

##### a. Description of the radars

The DOW mobile radars (Wurman et al. 1997; Wurman 2001) were developed for the express purpose of

obtaining high-resolution data in tornadoes and other small-scale and short-lived phenomena. The DOWs can scan rapidly, up to  $60^\circ \text{ s}^{-1}$ , produce transmit pulses of  $<100 \text{ ns}$ , and sample received signals as frequently as every 83 ns to obtain nonoversampled range resolution as low as 15 m (12.5 m oversampled). The DOWs operate at 9.3 GHz, with a peak transmitted power of 250 kW. The 2.44-m parabolic antennas produce beam widths of  $0.93^\circ$ , typically oversampled every  $0.3^\circ$  in the horizontal.

##### b. Targeting of storm A' and single-Doppler observations

At approximately 2310 UTC, the DOW2 and DOW3 radars targeted supercell storm A near Sapulpa, Oklahoma. As the DOWs drove south of Sapulpa (Fig. 4), radar data indicated strong rotation at 2333 UTC, and a funnel cloud was first noted visually at 2334 UTC and was visible as a cone-shaped lowering partially ob-

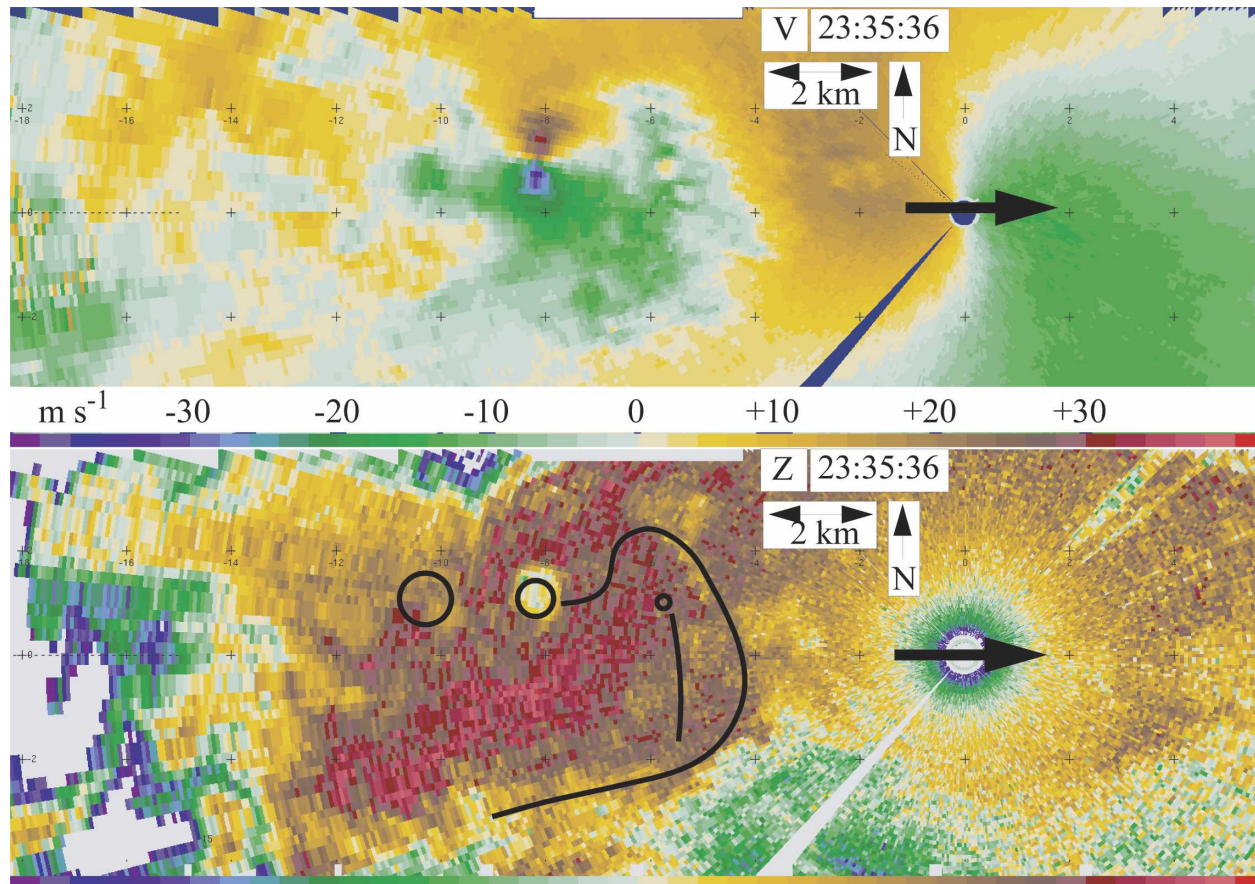


FIG. 5. First DOW observations of Kiefer tornado, 2335:36 UTC. (top) Doppler velocity and (bottom) uncalibrated radar reflectivity from DOW3 in ongoing tornado. Intense velocity couplet and low-reflectivity eye demark the tornado. Regions of apparent cyclonic and anticyclonic vertical vorticity to west and east of tornado indicated with circles. Approximate location of the gust front indicated with serpentine line. Range ticks are spaced at 2 km. Scan elevation is approximately  $4^\circ$ . DOW is in motion, skewing Doppler velocities. Apparent low-reflectivity near radar due to receiver saturation. DOW motion indicated by arrow at radar origin.

scured by rain. The National Weather Service listed two separate tornadoes, both rated F1 on the Fujita scale (Fujita 1975; more information available online at <http://www.srh.noaa.gov/oun/tornadodata/county/getcounty.php?county=Creek>) one occurring only at 2335 UTC, the other from 2338 to 2345 UTC. Continuous DOW observations beginning at 2335 UTC (discussed below), suggest that these reports represented a single tornadic circulation, with a visible condensation funnel intermittently in contact with the ground.

The DOWs began recording data at 2335:36 UTC (Fig. 5). Scans at  $4.3^\circ$  elevation crossed the tornado at 600 m AGL. The Doppler velocity difference,  $\Delta V$ , across the tornado was  $65 \text{ m s}^{-1}$  ( $+33, -32$ ). However, it is likely that the actual velocities on the southern (inbound) side of the tornado were several meters per seconds higher since the DOW platform itself was moving eastward, away from the tornado, at approximately  $10 \text{ m s}^{-1}$ . It is also likely, based on DOW observations

of many other tornadoes (e.g., Wurman et al. 1996; Wurman and Gill 2000; Wurman 2002; Alexander and Wurman 2005; Lee and Wurman 2005) that more intense winds occurred below the observed 600 m AGL. The observed spatial scale of the tornado circulation, from peak inbound to peak outbound Doppler velocity, was 660 m, but it is likely that a smaller embedded circulation representing the true tornado went unobserved (Wurman and Alexander 2004). The implied vertical vorticity, assuming axisymmetry, across the measured core flow region was estimated by calculating twice the Doppler difference divided by the distance across the measured core flow region, or  $2 \times (64.8 \text{ m s}^{-1}) / (660 \text{ m}) = 0.2 \text{ s}^{-1}$ , which was a low value, but one not atypical in tornadoes observed with similar resolution (Wurman et al. 1996; Wurman and Gill 2000; Wurman 2002; Alexander and Wurman 2005; Lee and Wurman 2005). The DOW radar sweep crossed through the tornadic region of storm A at 600 m AGL,

near the altitude of a nearly contemporaneous WSR-88D sweep at 500 m AGL (Fig. 3c). While the beamwidth of the KINX radar was much larger, over 900 m, the DOW and KINX fields, revealing the Doppler velocity ( $V$ ) couplet associated with the tornado, were relatively consistent, although the velocity difference across the KINX velocity couplet was somewhat smaller and many details were smoothed (e.g.,  $\Delta V_{\text{DOW}} = 65 \text{ s}^{-1}$ ,  $\Delta V_{\text{KINX}} = 49 \text{ s}^{-1}$ ,  $\text{Vorticity}_{\text{DOW}} = 0.2 \text{ s}^{-1}$ ,  $\text{Vorticity}_{\text{KINX}} = 0.1 \text{ s}^{-1}$ ).

In the DOW data, a weak anticyclonic Doppler velocity couplet was present 2.5 km east of the tornado, with a velocity difference across the feature of  $<20 \text{ m s}^{-1}$ . A weak and broad cyclonic circulation was present 3.1 km to the west of the tornado. A crenellated zone of implied convergence, delineating the gust front, extended northeast of the tornado and then curved around, crossing the tornado's longitude approximately 3.8 km to the south. Of these features, only the gust front was evident in the KINX data.

An examination of the DOW radar reflectivity fields reveals a substantial region of precipitation, the remains of the merging storm B, surrounding the tornado, which was consistent with visual observations that the tornado was obscured by rain. A lower-reflectivity region with a diameter of nearly 1000 m was associated with the tornado, but was not likely the true eye feature of the smaller tornadic circulation (Wurman and Alexander 2004). Subsequent DOW scans revealed a double-eyewall structure observed by DOWs in other tornadoes (e.g., Wurman and Alexander 2004). The region behind the gust front was almost completely associated with high reflectivity, suggesting that this air was wet and presumably evaporatively cooled to some extent, with likely implications for the ability of the tornado to persist (Markowski et al. 2002).

Approximately 200 s later, at 2338:29 (Fig. 6) and 2339:00 UTC (not shown), the inner reflectivity ring is clearly distinct in the DOW data, with a diameter of approximately 500 m, and well separated from the inner edge of the previously observed "eye," which continues to have a diameter of 1000 m. The diameter of the core flow region was observed to be only about 220 m. Peak Doppler velocities, nearly uncontaminated by the now northward motion of the DOW3 truck, increased to  $47 \text{ m s}^{-1}$  at 400 m AGL, with a  $\Delta V$  across the tornado of  $90 \text{ m s}^{-1}$ , and an implied vorticity of over  $0.8 \text{ s}^{-1}$ , now a relatively high value for a moderate intensity tornado sampled at this distance.

### c. Dual-Doppler deployment

The first ever dual-Doppler deployment by ground-based mobile radars near a tornado commenced at 2339

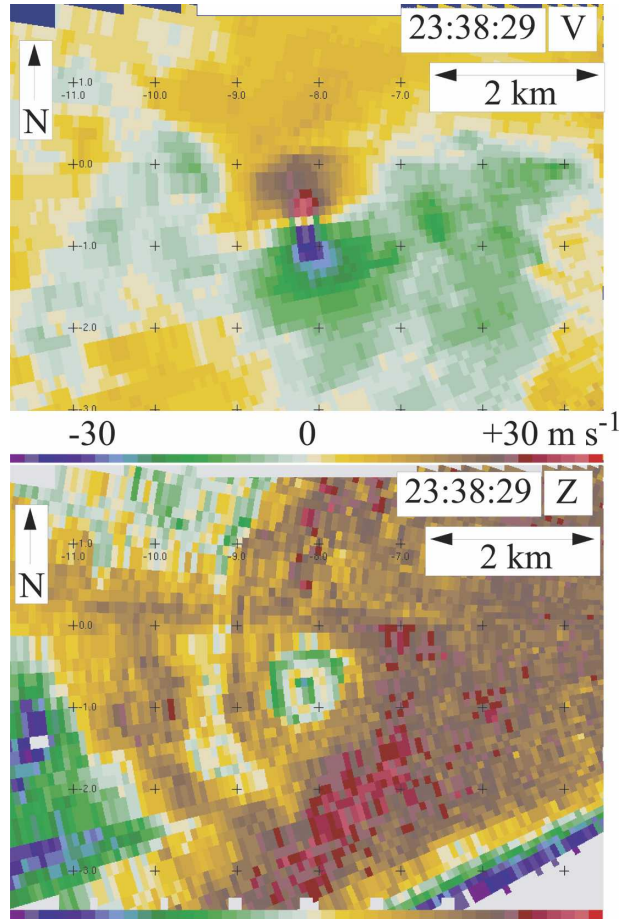


FIG. 6. DOW observations of tornado immediately before dual-Doppler deployment: 2338:29–2339:00 UTC. (top) Doppler velocity and (bottom) uncalibrated radar reflectivity from DOW3. Inner reflectivity eye is now visible, revealing aliased nature of larger, 1000-m-diameter eye. Tornado has intensified and is surrounded by precipitation from merging storm B, and is not associated with a hook echo reflectivity structure. DOW is in motion roughly perpendicularly to tornado, so Doppler velocities are not skewed significantly. Tick marks are at 1-km intervals.

UTC near Glenpool, Oklahoma, with DOW3 to the north and DOW2 to the south, defining a 5.37-km baseline oriented along  $174.9^\circ$  (see Fig. 4). Site selection was difficult, and low-level blockage of radar beams by both foliage and buildings was a problem. During the deployment, the tornado was still visible to the west from the DOW2 site as a condensation funnel in the shape of an inverted truncated cone (Fig. 7), but was becoming surrounded by rain and becoming nearly completely obscured visually.

During the dual-Doppler observation period, the tornado was approximately 9.4 km from DOW2 and 7.8 km from DOW3. The beam-crossing angle of the ra-



FIG. 7. Tornado near Kiefer, OK, as viewed from DOW2 at site "a" during dual-Doppler deployment at 2340 UTC 26 May 1997.

dars, at the tornado, was  $35^\circ$ , increasing to  $60^\circ$  at the easternmost extension of the gust front. These beam-crossing angles were sufficiently large to permit accurate dual-Doppler calculations.

Due to limitations of the early DOW hardware (Wurman et al. 1997), subsequently corrected (Wurman 2001), both antenna systems were only partially functional and were able to collect data in only two dimensions during a limited period during the deployment, resulting in about 60 s of spatially and temporally overlapping coverage. Observations taken at other times by the two radars occurred at different altitudes near the tornado and, thus, were unsuitable for accurate dual-Doppler analyses. As is critical for accurate dual-Doppler retrieval, the two DOWs were leveled precisely during the deployment, resulting in antenna pointing accurate to within  $0.2^\circ$ .

During the period of synchronized scanning, the DOWs conducted survey-type scans through a full  $360^\circ$  range of azimuths, at approximately  $28^\circ\text{--}30^\circ\text{ s}^{-1}$ , repeating every 12–18 s. The data were collected at an altitude centered close to 600 m AGL at the range of the tornado to the respective radars. The difference in altitude of the DOW2 and DOW3 beams at the tornado was less than 50 m, or less than 1/2 the beamwidth, during the period considered suitable for dual-Doppler analysis. While the beam altitudes varied throughout the dual-Doppler domain, they were typically 300–600 m AGL in the regions of primary interest discussed below. Importantly, the differences in the beam altitudes of the two radars were less than 100 m in the region of the gust front, rear-flank downdraft, and other features discussed below, with the exception of the southern extension of the gust front as it ap-

proached DOW2. Processing with  $0.25\ \mu\text{s}$  (sometimes  $0.375\ \mu\text{s}$ ) gates using a  $250\text{-}\mu\text{s}$  transmit pulse resulted in 75-m (sometimes 112-m) range resolution. Pulse-pair processing produced 60 integrated beams per second, resulting in azimuthal oversampling by a factor of 1.5–3.0 enhancing azimuthal resolution (Wood et al. 2001) limited by the 130- (DOW3) to 150-m (DOW2) beamwidths at the range of the tornado.

The result of these data collection modes are two-dimensional-only fields of Doppler velocities through the tornado and surrounding storm with oversampled resolutions of approximately  $75\text{ m} \times 70\text{ m} \times 70\text{ m} \times 14\text{ s}$ , resulting in spatial resolution of  $4 \times 10^5\text{ m}^3$ , and temporal-spatial resolution of  $5 \times 10^6\text{ m}^3\text{ s}$ . Data from the period 0340:10–0341:00 UTC are suitable for dual-Doppler analyses. While limited to two dimensions, and to a short time period, just 50 s, these represent the highest temporal or spatial resolution dual-Doppler syntheses of a tornado and tornadic storm ever produced. Experiments in subsequent years have yielded 3D and 4D dual-Doppler fields in several tornadoes (e.g., Richardson et al. 2001; Dowell et al. 2002; Wurman et al. 2007b).

At the beginning of this period, scans that passed through the tornado at 2340:15 (DOW2) and 2340:21 (DOW3; Fig. 8) revealed a moderately intense tornado with winds in excess of  $40\text{ m s}^{-1}$  at 600 m AGL. The Doppler velocity difference across the tornado was over  $81\text{ m s}^{-1}$  over a distance of approximately 200 m, resulting in implied vertical vorticity of  $0.8\text{ s}^{-1}$ . The gust front continued to wrap around from northeast of the tornado to southeast of the tornado. These general features were also discernible in the coarser KINX fields (Figs. 3c,d). A double gust front structure was visible in the velocity fields and was associated with enhanced gradients in reflectivity. There was a region of slightly enhanced shear approximately 3 km to the east of the tornado, but the evidence for this feature in the raw Doppler data is subtle. The nature of this feature is revealed by the dual-Doppler analysis discussed below. The anticyclonic circulation observed earlier to the east of the tornado had dissipated as had the cyclonic circulation to the west. The inner eyewall structure has persisted. While attenuation of the radar beams affected the appearance of the reflectivity field, both radars were able to obtain accurate Doppler velocity data throughout the tornadic region and surrounding areas of the storm, even through several kilometers of heavy rain. The larger-scale structures surrounding the tornado evolved little during the short dual-Doppler study period, as evidenced by the nearly identical structures present in the raw data from sweeps through the tor-

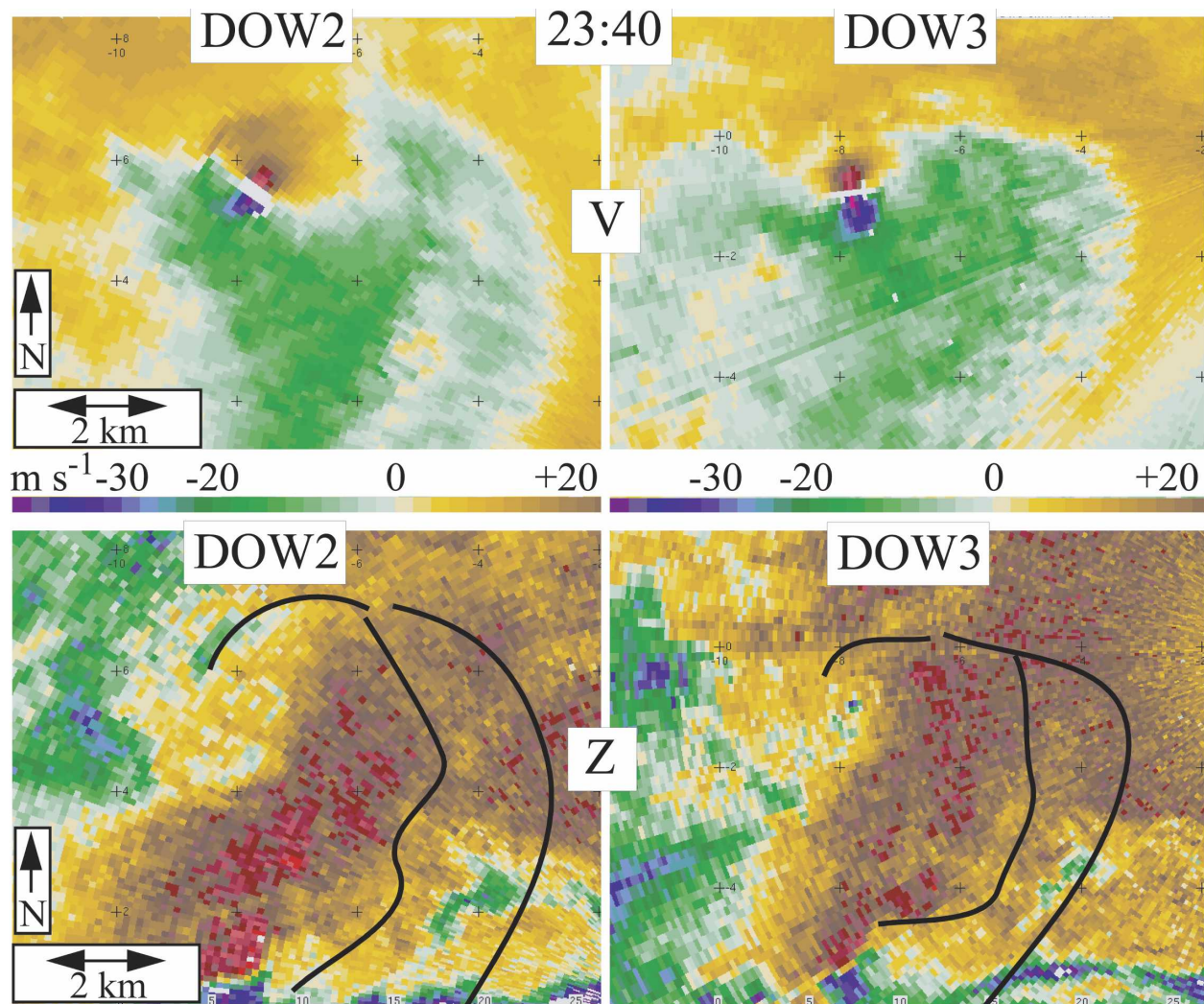


FIG. 8. Raw radar fields at start of dual-Doppler study period: 2340 UTC. (left) DOW2 and (right) DOW3 (top) Doppler velocity and (bottom) uncalibrated radar reflectivity. Location of the gust fronts, as subjectively and independently determined from each radar's data, are shown. Tick marks are at 1-km intervals. Intense Doppler velocity couplets and similar radar reflectivity and Doppler fields are evident.

nado by DOW3 at times closer to the end of the dual-Doppler period at 2341 UTC (Fig. 9).

#### d. Dual-Doppler syntheses

Using the locations of common weather and clutter targets, including the low-reflectivity eye of the tornado, the small intense Doppler velocity couplet in the tornado, and other features, the pointing angle of each DOW is precisely determined to within  $0.2^\circ$  and the azimuths of the DOW data are corrected. Data are then interpolated onto Cartesian grids. A grid spacing of  $100 \text{ m} \times 100 \text{ m}$  with areas of  $10^4 \text{ m}^2$ , approximately equal to the native 2D radar resolution is chosen and a

Cressman interpolation with a horizontal radius of influence of 400 m is used. The data included in each dual-Doppler synthesis span only 12–18 s, resulting in maximum differences in sampling times by each radar near the tornado of 6 s. The translational speed of the tornado, as determined by tracking the center of the DOW-measured Doppler velocity couplet, is approximately  $0.9\text{--}4.5 \text{ m s}^{-1}$  during the dual-Doppler analysis period resulting in a worst-case differential translation of  $(4.5 \text{ m s}^{-1}) \times (6 \text{ s})$  or 27 m, about  $\frac{1}{4}$  grid point, which was insignificant and neglected.

Four completely independent dual-Doppler syntheses, with nominal times of 2340:14, 2340:28, 2340:40, and 2340:53 UTC were created.

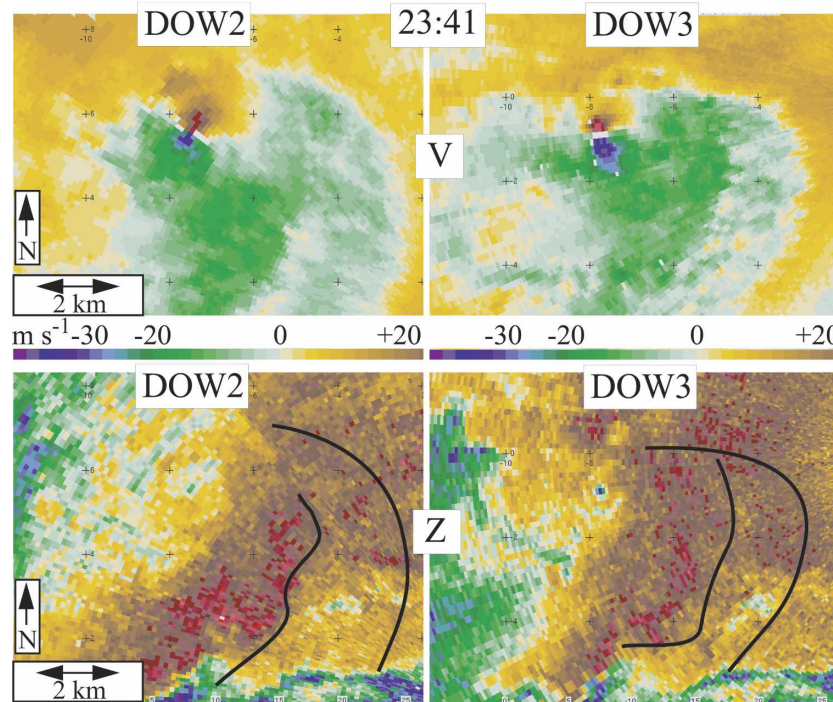


FIG. 9. Raw radar fields at end of dual-Doppler study period: 2341 UTC. Fields and annotation same as in Fig. 8.

## 5. Dual-Doppler analyses and discussion

### a. Verification of stability of dual-Doppler wind fields

The dual-Doppler vector wind field retrievals revealed several important features of the tornadic storm with unprecedented observational detail. While the 100-m grid spacing of the syntheses precluded precise retrieval of the details of the core flow region of the tornado itself (Carbone et al. 1985), much of the tornadic flow was, in fact, resolved (Fig. 10). A spatially aliased nearly symmetric representation of the core flow region with a diameter of 500–600 m with peak velocities of over  $60 \text{ m s}^{-1}$  was retrieved in all four independent dual-Doppler fields. The velocities to the north and south of the tornado were near  $50 \text{ m s}^{-1}$ , which was very consistent with the peak Doppler velocities measured by the individual DOWs. Peak-retrieved vertical vorticity in the spatially aliased tornado was  $0.30 \text{ s}^{-1}$  at 2340:14 UTC, which was less than that estimated from the raw Doppler data and more representative of the slightly larger scale retained in the objective analysis. Peak vertical vorticity at 2340:28, 2340:40, and 2340:53 UTC (Fig. 11), varied generally from 0.25 to  $0.26 \text{ s}^{-1}$ , peaking at  $0.30 \text{ s}^{-1}$ . The remarkable consistency of these values and the structure of the vorticity field immediately surrounding the tornado

lend credibility to the validity of the dual-Doppler analyses and the stability of the features being analyzed. While the spatially aliased nature of the dual-Doppler retrieval of the core flow of the tornado precludes its use to study the structure of the tornado itself, the realistic, if smoothed, characteristics of the retrieval imply that the retrieval is of sufficient quality to enable study of larger-scale features surrounding the tornado. Syntheses using data at different times that were collected at different elevations from each DOW did not yield this repeatability indicating that data from different levels cannot be combined in dual-Doppler syntheses in the highly sheared environment near tornadoes. Small changes of  $\frac{1}{2}$  beamwidth in azimuthal navigation caused significant changes in the retrieved fields, indicating that precise navigation is necessary for reliable dual-Doppler syntheses. *While imprecisely navigated dual-Doppler analyses will always produce vector wind fields, these wind fields are not reliable.*

### b. Resolved storm structures

Structures surrounding the tornado, including the rear-flank downdraft (RFD), gust front, and updraft region, are clearly resolved in the dual-Doppler analyses, Figs. 12–13. The overall structure is remarkably similar to that of conceptual models (e.g., Lemon and Doswell 1979) and to those generated in computer

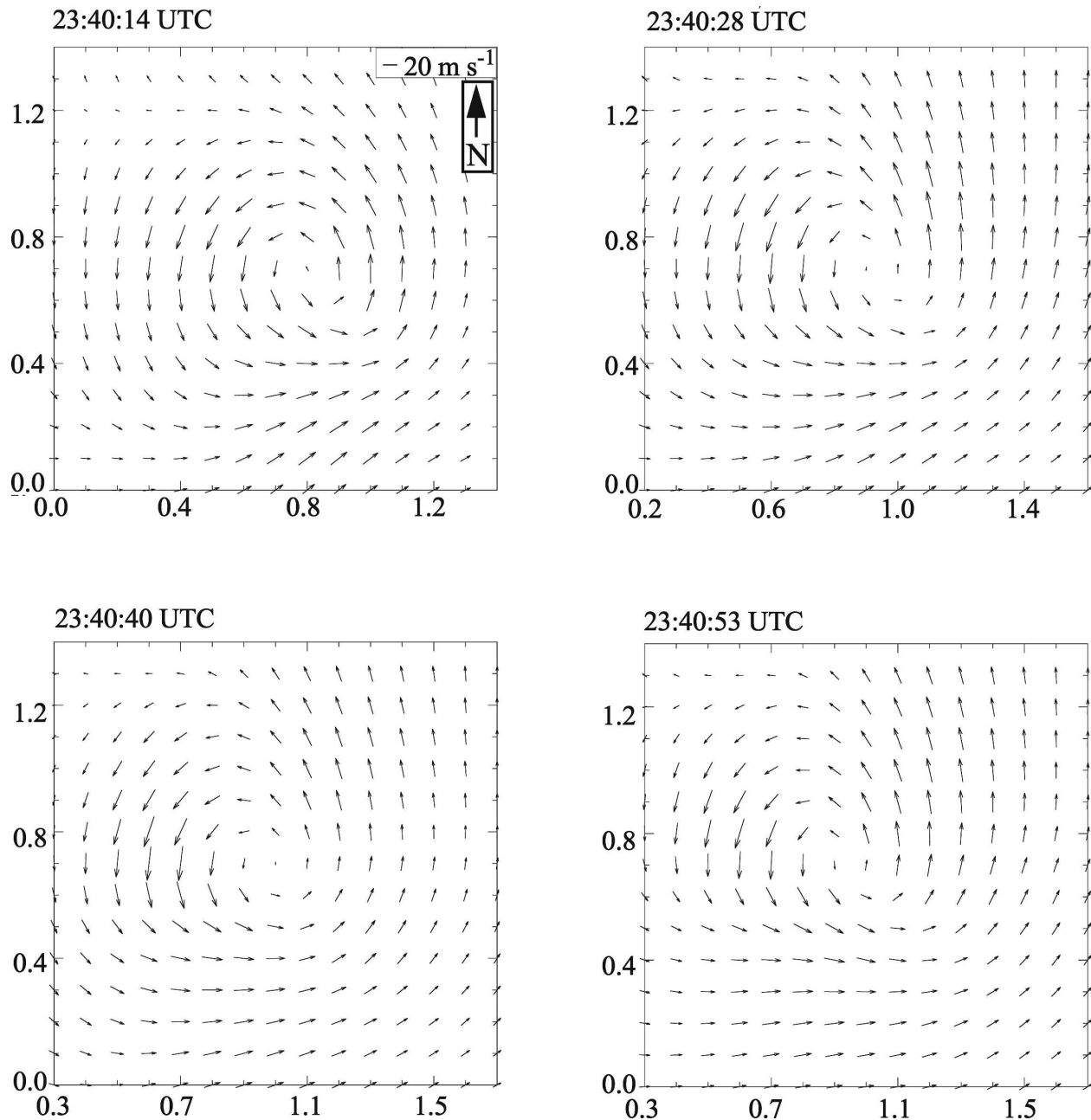


FIG. 10. Dual-Doppler vector wind field calculations in the immediate vicinity of the tornado. A  $20 \text{ m s}^{-1}$  vector scale shown top right of top left panel. Peak wind speeds remain near  $60 \text{ m s}^{-1}$  in all four independent dual-Doppler analyses. Scale markings in km. Times are in UTC.

simulations (e.g., Wicker and Wilhelmson 1995; Adlerman et al. 1999; Adlerman 2003), as discussed below. The tornado exists at the boundary between convergence and divergence, presumably at the boundary between upward- and downward-moving air. A region of divergence and negative vertical vorticity is wrapped around the tornado from west to south, then to the east of the tornado. This region is observational evidence of

the RFD. In this case, the RFD wrapped around the east side of the tornado, cutting off surface inflow into the tornado, consistent with a full occlusion process in a mature, soon to dissipate tornado (Wicker and Wilhelmson 1995). A gust front, revealed as a region of cyclonic vorticity and convergence, wraps around the tornado, consistent with Brandes (1977), (1978), (1984b), and others. A double gust front structure is



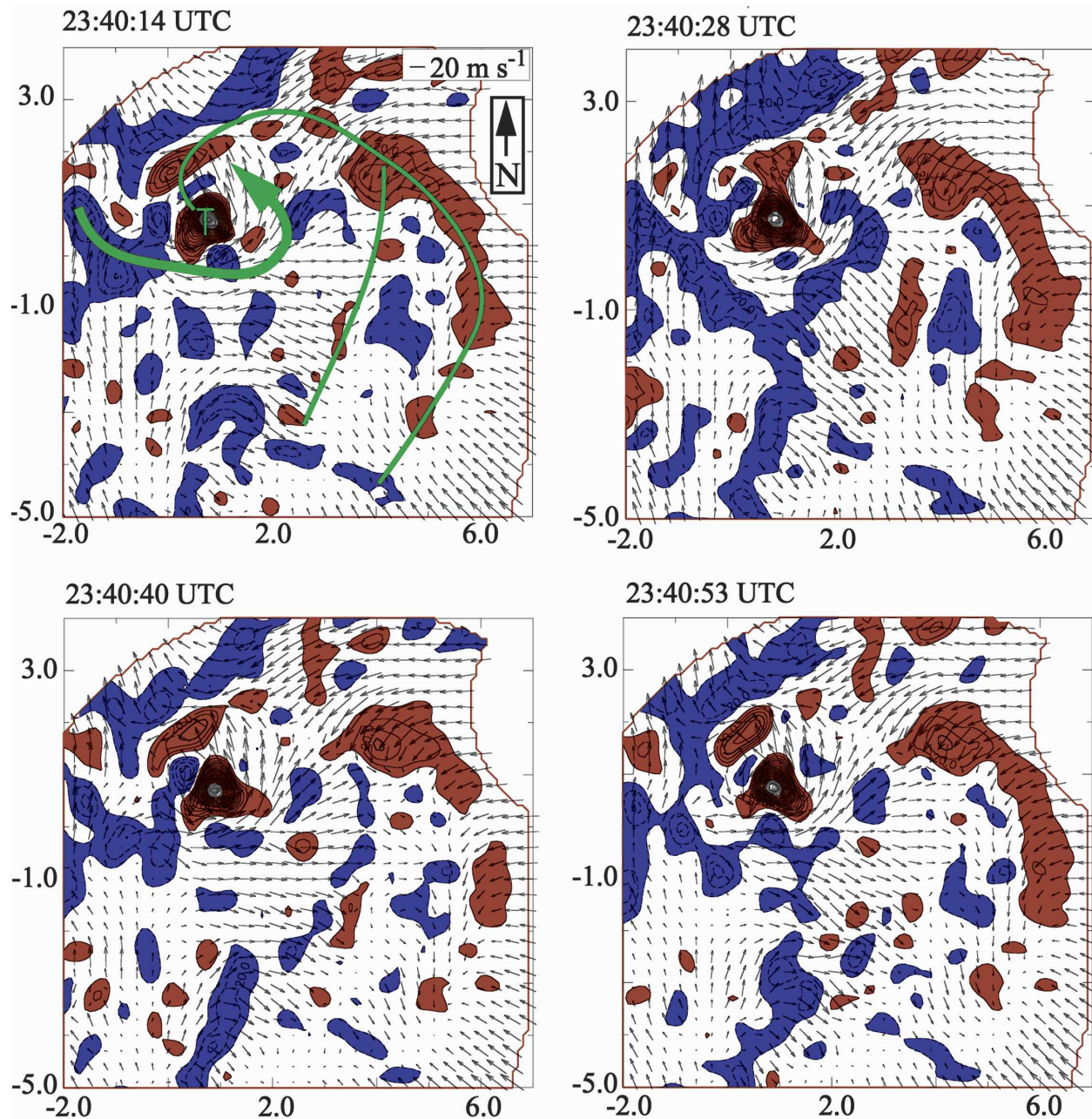


FIG. 12. Vertical vorticity in tornadic region of storm in each of four independent dual-Doppler syntheses. Contour interval is  $20 \times 10^{-3} \text{ s}^{-1}$ . Cyclonic vorticity (red) associated with the tornado and the region to the east are consistent in all fields, as is the general region of anticyclonic vorticity (blue) associated with the RFD wrapping around the tornado. Vectors have been thinned for presentation. Vector scale at top right of top left panel. Scale markings are in km. Times are in UTC.

dence in the currently analyzed fields is enhanced due to their repeatability in several different dual-Doppler analyses that are derived from completely different input data. Both the first order (i.e.,  $u, v$ ), and the derivative (i.e.,  $\nabla \times \mathbf{V}, \nabla \cdot \mathbf{V}$ ) fields in these analyses exhibit repeatable large-scale features as shown in the various time panels in Figs. 12–13. These include the double

gust front structure, the negative vorticity in the wrapping RFD, the enhanced vertical vorticity to the east of the tornado, and even smaller-scale measures such as peak tornado vorticity. Features with scales much less than 1 km, such as small-scale fluctuations of vorticity and convergence along the gust fronts and RFD, are intermittent and do not persist from analysis to analy-

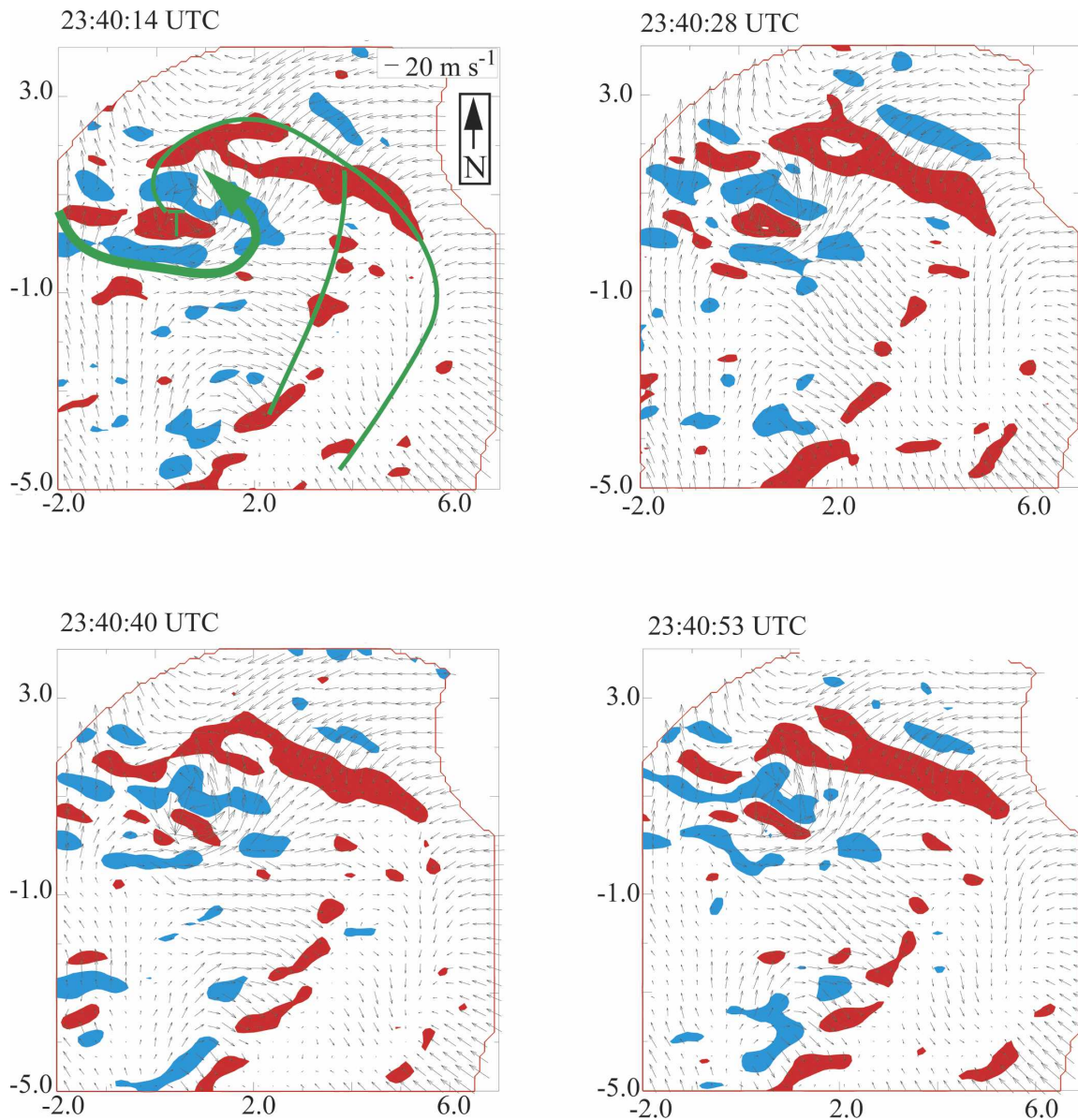


FIG. 13. Divergence (blue) and convergence (red) in tornadic region of storm in each of four independent dual-Doppler syntheses. Divergence is associated with the RFD as it wraps around the tornado. Convergence is present in the gust fronts and is maximized in the region to the east of the tornado near where the gust fronts intersect. Vectors have been thinned for presentation. Vector scale at top right of top left panel. Scale markings are in km. Times are in UTC.

sis. These may be transient, or merely artifacts of the analyses. In the absence of corroborating evidence, prudent skeptics would assume the latter.

With detailed vector wind fields retrieved, it is possible to calculate the total circulation in the area surrounding the tornado, at least at the one level observed. The amount of circulation in the tornadic circulation, calculated at a radius of 1.4 km from the tornado center, remained nearly constant during the observation period, with values between  $1.06$  and  $1.20 \times 10^5 \text{ m}^2 \text{ s}^{-1}$ .

This was the same order of magnitude as that calculated in a simulated tornadic storm (Wicker and Wilhelmson 1995).

### c. Cyclic tornadogenesis

In simulations of cyclic tornadogenesis (Adlerman et al. 1999) enhanced vertical vorticity and updraft is found to the east of a maturing/dissipating tornado. Thus, it is tempting to draw such a link between the enhanced vorticity region observed to the east of the

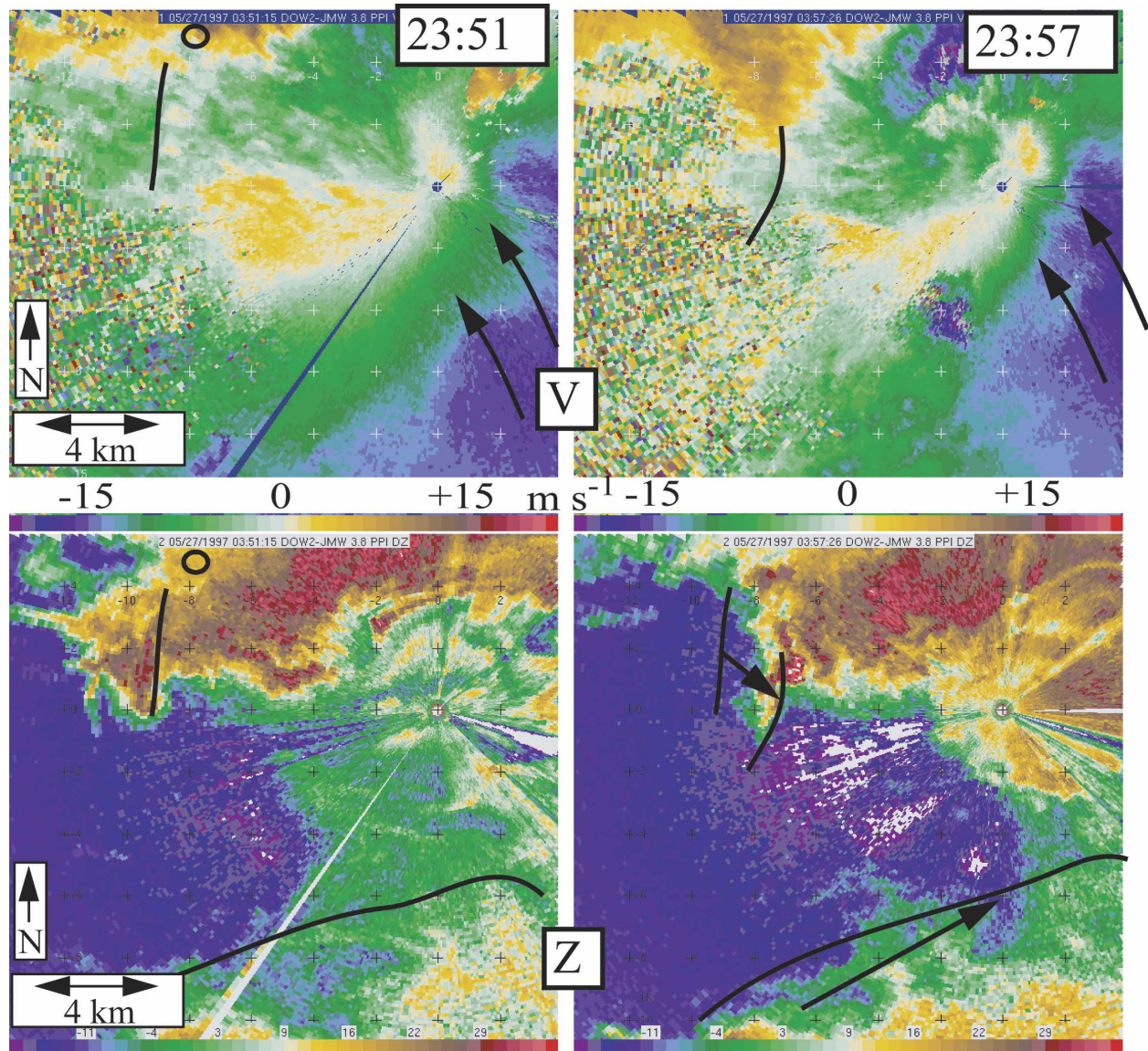


FIG. 14. Evolution of storm A' between tornadoes. (left) Dissipated Kiefer tornado is indicated with black circle (2351 UTC). (right) By 2357 the reflectivity line and wind shift propagate eastward toward the region of enhanced cyclonic shear.

weakening Kiefer tornado and the genesis of another tornado, described below, that was observed by the DOWs several hundred seconds later near Glenpool. However, the relationship between the observed large vorticity region and the subsequent genesis of the Glenpool tornado was not clear due to limitations in the continuity of the DOW observations, their largely two-dimensional nature, and complications introduced by a subsequent merger of storms A' and C.

## 6. Tornadogenesis during merger with storm C

By 2348 UTC, the Kiefer tornado dissipated to the west of the core of the supercell, well separated from

the updraft region. At the time of dissipation, the enhanced vorticity region, manifested as a region of increased cyclonic shear in the Doppler velocity field, persisted to the east-northeast of the tornado.

There was no evidence of low-level rotation, nor evidence of any storm structures unambiguously associated with a new tornadogenesis during the several minutes after dissipation, either in DOW or KINX data (Figs. 3f,g). The old center of circulation was visible in the DOW data at 2351 UTC (Fig. 14), while a slight enhancement of low-level rotation was present to its southeast. The region of enhanced shear was moving southward. A Doppler velocity shift and reflectivity

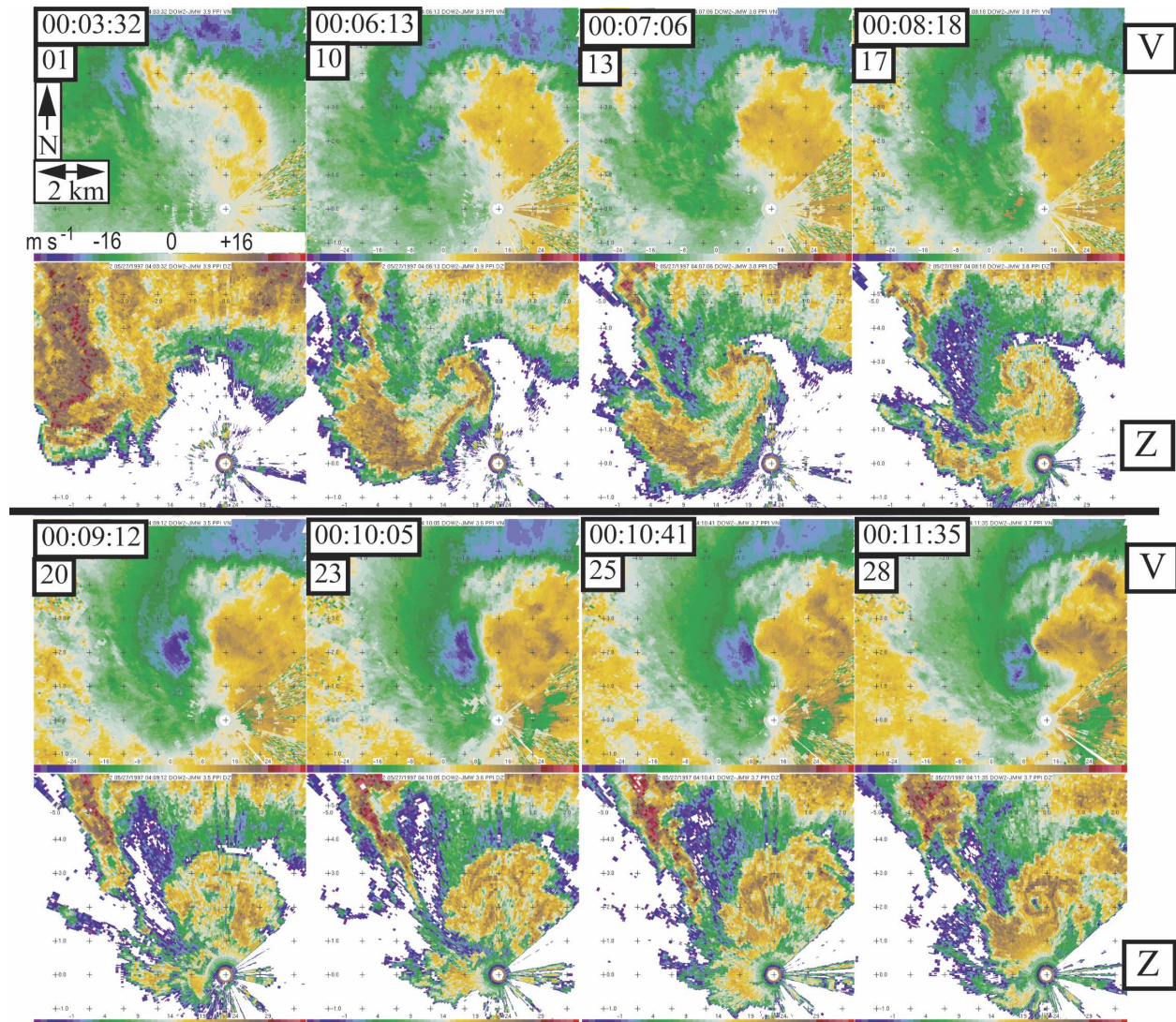


FIG. 15. The genesis of the Glenpool tornado: (top) Doppler velocity and (bottom) uncalibrated radar reflectivity during genesis of the Glenpool tornado. Time of each sweep through tornado and sweep number is indicated. Two phases of scale contraction and intensification occur during tornadogenesis. Velocity scale for all velocity panels is shown in panel for sweep “01.”

protuberance, possibly associated with a new gust front/RFD push, was moving rapidly eastward during 2351–2357 UTC. During this period storm C began to merge with storm A' (Figs. 3f–i). By 0001 UTC, there is evidence in the KINX data of a region of strong convergence, approaching  $0.02 \text{ s}^{-1}$ , associated with the interaction of the air moving north from the northern flank of storm C and the air moving out from the forward flank of storm A' (Figs. 3h,i). Also by 0001 UTC, KINX data revealed that the circulation aloft had intensified and contracted.

Unfortunately, there were no low-level observations by either DOW during the critical period from 2358 to 0003 UTC. By 0003 UTC, DOW data (Fig. 15) revealed

that a tornadogenesis was well underway and the low-level rotation had increased significantly. A new hook echo had formed and a broad region of strong shear, with a  $\Delta V$  of over  $30 \text{ m s}^{-1}$  over 700 m, implying a vertical vorticity of  $0.08\text{--}0.10 \text{ s}^{-1}$ , was present. Both radars had redeployed to the sites labeled “b” (Fig. 4) by 0004 UTC.

Two-dimensional single-Doppler data with very fine spatial and temporal resolution were collected during this tornadogenesis event. The DOW2 radar conducted  $360^\circ$  sweeps through the genesis region at  $20^\circ \text{ s}^{-1}$ , repeating every 18 s from 0003 to 0012 UTC, resulting in 28 independent slices. The sweeps were conducted at an elevation angle of  $3.5^\circ\text{--}3.9^\circ$  resulting in slices

through the genesis region at 300 m AGL at 0003 UTC, decreasing to 140 m AGL after 0010 UTC, by which time a tornado had formed. DOW2 resolution volumes were  $75 \text{ m} \times 65 \text{ m} \times 65 \text{ m}$  ( $3 \times 10^5 \text{ m}^3$ ) decreasing to  $75 \text{ m} \times 33 \text{ m} \times 33 \text{ m}$  ( $8 \times 10^4 \text{ m}^3$ ), and these were further reduced by oversampling.

At 0003:39 UTC, a broad region of apparent cyclonic shear was seen to be moving south southwest and was associated with a blunt protrusion of reflectivity. Peak Doppler velocities in this feature, at 300 m AGL, were only  $22 \text{ m s}^{-1}$ , with a  $\Delta V$  of  $33 \text{ m s}^{-1}$ . Strong convergence in the storm updraft was visible to the northeast of the shear region. Shear across the tornadogenic circulation, the scale of the circulation, and estimated vertical vorticity were calculated for every sweep during the genesis (Fig. 16). During the several minute period, from 0003 UTC until an unambiguous tornado exists after 0010 UTC, the evolution of the scale and intensity of the circulation did not proceed monotonically. The Doppler velocity difference across the most intense portion of the circulation decreased or remained steady, with  $\Delta V$  values primarily between 27 and  $36 \text{ m s}^{-1}$ , until the final minute of genesis. A region of strong inbound Doppler velocities moved southeastward, toward the DOW2 radar, from 0003 to 0007 UTC, but the intensity of the inbound velocities decreased significantly (Fig. 15). The scale of the nascent circulation, defined as the distance between the location of the peak inbound and peak outbound Doppler velocities, contracted from 1000 m in diameter at 0003 UTC to less than 400 m at 0007 UTC, resulting in an increase in vertical vorticity from below  $0.1 \text{ s}^{-1}$  early in this period to over  $0.15 \text{ s}^{-1}$  just after 0007 UTC. The hook echo extended distinctly from the core of the supercell by 0006 UTC, connected by only a <100-m-thick tendril of high reflectivity. The intensifying circulation was associated with a coiling of the tip of the hook echo. (Data from KINX, Fig. 3i, suggested that a hook with a bulbous tip had formed and that the circulation had intensified, but the details of the rapid and small-scale evolution were missing.) The apparent convergence to the east and northeast of the developing tornado had continued to intensify as did the northward airflow between storms A' and C. By 0008 UTC DOW data show hints of a developing eye feature inside the tip of the coil. However, this tightening circulation did not become the tornado.

By 0009 UTC, the vortex broadened and weakened and another region of strong inbound velocities had begun to move southeastward toward the radar. This second pulse developed into the eventual tornado. The  $\Delta V$  values gradually increased to over  $40 \text{ m s}^{-1}$  and the scale of the new circulation decreased to 400 m by 0010

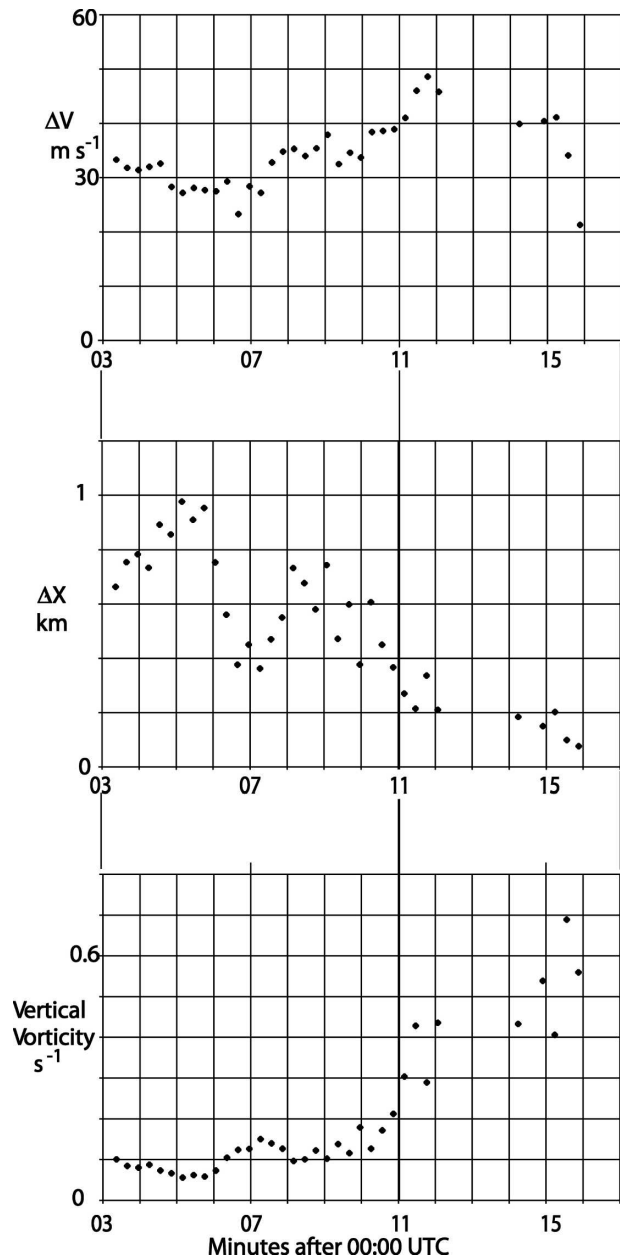


FIG. 16. Evolution of Doppler velocity difference, spatial scale, and estimated vertical vorticity in the Glenpool tornado. Two phases of scale contraction and intensification occur during tornadogenesis.

UTC and 200 m by 0012 UTC. Vertical vorticity increased rapidly after 0010 UTC, from below  $0.2 \text{ s}^{-1}$  to over  $0.4 \text{ s}^{-1}$  by 0012 UTC. The reflectivity structure of the coil feature reflected the complexity of the wind field's evolution. From 0009 to 0010 UTC, no clear central eye existed and several small and transient eyelike features appeared and disappeared as raindrops were centrifuged (Dowell et al. 2005). By 0011 UTC, the final eye of the tornado became visible and the hook echo

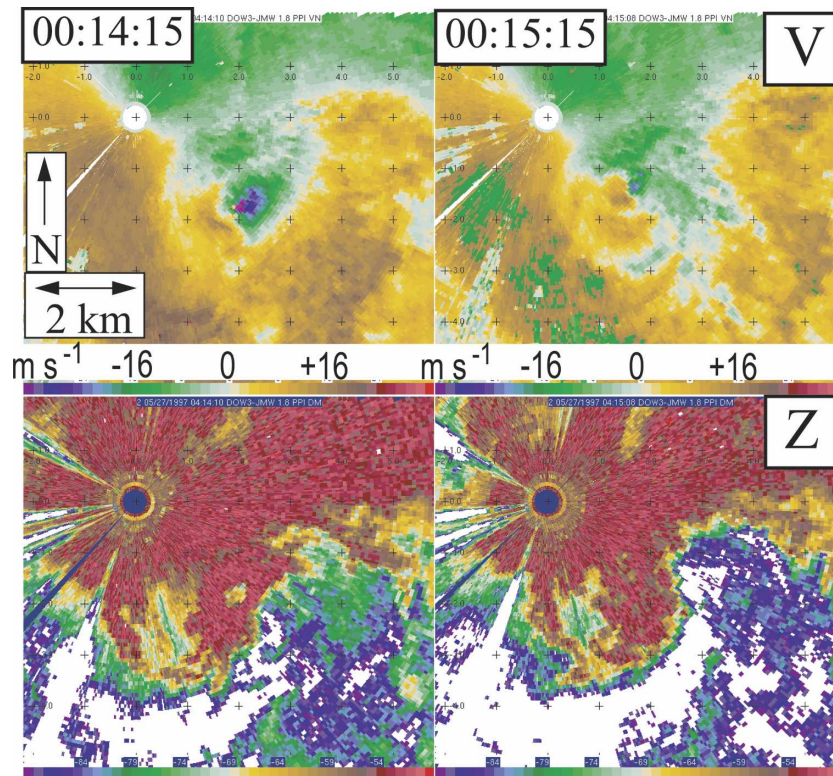


FIG. 17. The mature and dissipating Glenpool tornado: (top) Doppler velocity and (bottom) uncalibrated radar reflectivity during genesis of the Glenpool tornado. Scale and key are the same as in Fig. 15.

with a coiled tip containing the eye assumed a structure commonly found in tornadoes (e.g., Wurman and Gill 2000). The National Weather Service logged a tornado from 0008 to 0015 UTC, which was rated F0 (more information available online at <http://www.srh.noaa.gov/oun/tornadodata/county/getcounty.php?county=Creek>) based on damage to a manufactured home.

As the tornado approached within 2 km of DOW2, the radar redeployed to the southeast, to site “c” (Fig. 4). By the time it redeployed, at 0015 UTC, the tornado had dissipated. Fortunately, the tornado moved out from behind a blocked location with respect to DOW3, still at its site b, and a few low-level scans were collected after 0014 UTC. At 0014:15 UTC (Fig. 17), the tornado was mature, with peak Doppler velocities of  $37 \text{ m s}^{-1}$  at the scanned level of 86 m AGL, which was reasonably consistent with its rated F0 intensity. The reflectivity structure was typical of a maturing and weakening tornado and the coil at the tip of the hook folded back north to be in contact with the main reflectivity region associated with the core of the supercell. There was no obvious convergence near the tornado, suggesting that the tornadic circulation had occluded. Sixty seconds later (Fig. 17), the tornado had nearly dissipated. Peak

$\Delta V$  across the circulation was  $34 \text{ m s}^{-1}$  and was rapidly decreasing, the low reflectivity eye had filled, and the hook echo as a whole was just a blunt protuberance, similar in appearance to the hook echo at 0003 UTC. In contrast to 0003 UTC, there was no strong southerly flow or zone of intense convergence near the hook echo. The lowest KINX sweep at 0016:57 UTC (Fig. 3k) still indicated a potentially tornadic circulation at 500 m AGL, but the proximate DOW data showed clearly that the tornado had dissipated. Intense precipitation from storm C had approached to within 5 km of the dissipating tornado.

The DOWs ended their deployments around 0020 UTC, but KINX data (Figs. 3k,l) revealed that the hook and low-level circulation continued to degrade and that storm A’ became disorganized because of its interaction with storm C.

## 7. Discussion and conclusions

The current study permits several conclusions to be drawn, and suggests others, concerning tornado studies, tornadic storm structure, and processes related to tornadogenesis and their possible results. Some of these

are self-evident from the previous descriptions and are merely listed below, some relating to tornadogenesis mechanisms require discussion.

Dual-Doppler deployments of mobile radars to study tornadic storm structure, while difficult, are possible. Data can be collected with sufficient resolution to resolve tornadic storm structures including the low-level RFD, gust fronts, and enhanced vorticity zones. Although only two-dimensional data were collected in this study, subsequent deployments have resulted in long duration three-dimensional fields, permitting more complete analysis of the vorticity budget of tornadoes, and these are currently being analyzed (e.g., Richardson et al. 2001; Dowell et al. 2002; Wurman et al. 2007b). Local terrain, flora, and structures can impact negatively on data quality.

Despite strong attenuation of the X-band (3 cm) radar transmissions, high-quality Doppler data can be obtained throughout the southern and western regions of even a very wet supercell that has ingested extra strongly attenuating precipitation due to a merger. The complete hook echo, RFD, gust fronts, and much of the supercell core can be resolved. The high sensitivity of the 3-cm DOWs, due in part to 250-kW transmitters and high gain antennas, and their unique temporal-spatial resolution, due to scan rates  $>50^\circ \text{ s}^{-1}$ ,  $0.93^\circ$  beams, and oversampling, permit uniquely high-resolution dual-Doppler retrievals of tornadic storms. While radars with longer wavelengths suffer less attenuation, the severe compromises in spatial resolution required at these wavelengths are shown not to be necessary when studying the tornadic regions of supercell storms.

At typical deployment distances, about 7–10 km from tornadoes, the core flow region of the tornado vortex itself is only marginally resolved, precluding dual-Doppler analyses of tornado structure except in possibly the largest tornadoes (e.g., the Mulhall, Oklahoma, tornado of 3 May 1999 discussed in Wurman 2002). Actual dual-Doppler studies of the structure of typical tornado vortices will require very short baselines, which may be so infrequently realized as to be unfeasible. The Ground Based Velocity Track Display (GBVTD; Lee et al. 1999; Bluestein et al. 2004; Lee and Wurman 2005) and other single-Doppler techniques (Alexander and Wurman 2005; Dowell et al. 2005) may be the only practical methods by which to study the wind field structure of tornado vortices.

The consistency of retrieved larger-scale structures in the carefully navigated two-dimensional dual-Doppler vector wind fields suggests that these features are genuine and not artifacts of the complex interpolation and dual-Doppler synthesis process. Furthermore, the realistic appearance of the tornado vortex, albeit aliased to

larger-scale than the actual tornado, lends confidence to the analysis of larger-scale structures surrounding the tornado. In this particular study, contamination of the dual-Doppler fields due to temporal evolution (Clark et al. 1980; Gal-Chen 1982) was nearly eliminated only through the unintentional, and arguably undesirable, use of two-dimensional scanning, which severely limited the ability to infer three-dimensional storm evolution.

The retrieved values of circulation agree closely with that of numerical simulations, lending confidence to both the retrievals and simulations of tornadoes.

The fine temporal-scale and fine spatial-scale processes involved in tornadogenesis are complex and cannot be resolved by low-resolution measurements. The 18-s temporal resolution scanning reveals that structures evolve very rapidly and nonmonotonically. The current study provides evidence of multiple phases or pulses of scale contraction, separated by  $\sim 100$  s. Scanning by radars that repeat only every  $\sim 60$  s will miss important details in these events, which will be aliased to longer time scales. Rapid scanning combined with very finescale spatial observations (Wurman and Randall 2001) is critical if these processes are to be observed.

The Kiefer tornado developed as storm A was merging with storm B, and then the tornado dissipated. The Glenpool tornado developed as storm A' was merging with storm C, then quickly dissipated. As storm A merged with storm B, storm A's mesocyclone aloft underwent significant intensification and scale contraction, and intensified convergence was observed. Subsequent to the merger, the tornado was surrounded by substantial precipitation originating from storm B, and no classical hook echo existed, even in finescale DOW observations. It is likely that air parcels ingested into the updraft of the resultant merged storm A' were cooled by this precipitation and that this interfered with tornado maintenance (Markowski et al. 2002). The tornado dissipated shortly after its observation by the DOWs and rotation at both low levels (observed by DOWs) and aloft (observed by KINX) dissipated. The reintensification (or new generation) of the mesocyclone and the generation of a new hook echo and surface rotation in the storm resulting from the merger, storm A', was during its merger with storm C, which was much larger and more intense than storm B. Intensifying convergence was again observed. Another short-lived tornado, the Glenpool tornado, formed and quickly dissipated. Dissipation of this tornado and the hook echo in storm A' occurred as precipitation and air likely cooled by that precipitation, impinged on the updraft region.

The observed repeated merger, tornadogenesis, then

quick tornado and mesocyclone dissipation process suggests that the merger process may be causative. The following hypothesis for the cause of the genesis and quick dissipation of the tornado is suggested. Storm merger can enhance or trigger tornadogenesis. Enhanced convergence evident in the KINX and DOW data east of the genesis of the Kiefer and Glenpool tornadoes may have increased stretching of existing low-level vertical vorticity. Trajectory calculations were not possible here, but Adlerman et al. (1999) and Wicker and Wilhelmson (1995) showed the area east or northeast of the low-level mesocyclone to be one source region for parcels entering the low-level mesocyclone and the tornado. However, subsequent to this initial aid in tornadogenesis, the merger leads to impinging of air that is likely cooled by precipitation, suppressing stretching. Furthermore, the disruption of the structures in supercells thought probably responsible for generating low-level vorticity in the first place also enhanced the tornado dissipation process. It is further hypothesized that, while storm mergers may enhance, or even cause, tornadogenesis, the resultant tornadoes are likely to be short lived.

However, the qualities of storm mergers vary significantly from event to event. Further study will be needed to explore the role of storm interaction geometry, the relative size and intensity of the merging storms, and other factors as to how they affect the enhancement of tornadogenesis potential and the role of this variability on tornado intensity or duration. High-resolution dual-Doppler data along with low-level thermodynamic data are needed to clarify the mechanisms responsible for any association between storm mergers and tornadogenesis.

While structures hypothesized to be associated with cyclic tornadogenesis (Adlerman et al. 1999), namely enhanced vorticity to the east of a maturing tornado, were resolved in the DOW dual-Doppler analysis, the long period of time between the dissipation of the Kiefer tornado (dissipated by 2348 UTC), and the beginning of the genesis process of the Glenpool tornado (begins at about 0004 UTC), a gap of nearly 1000 s, complicates any attempt to conclusively link the observed zone of enhanced low-level vertical vorticity with the genesis of the subsequent tornado. The merger of storms C and A' further complicates the drawing of any inference concerning the role of the enhanced vorticity region in the subsequent genesis near Glenpool. It is impossible to know whether cyclic tornadogenesis would have occurred in the absence of the storm merger and it is suggested that the merger process itself was involved in the genesis of the short-lived tornado near Glenpool.

*Acknowledgments.* The authors wish to acknowledge Herb Stein, David Dowell, Scott Richardson, and Swarn Gill, who along with Wurman and Weygandt crewed the DOWs during these difficult intercepts. We thank David Dowell for photographs of the tornado. This work was supported by National Science Foundation Grants 0437505, 0437512, and 0437898, and NSF Grant 9703032. The DOW radars were constructed with significant support and assistance from the National Center for Atmospheric Research and the National Severe Storms Laboratory and are operated by the Center for Severe Weather Research with support from the National Science Foundation.

#### REFERENCES

- Adlerman, E. J., 2003: Numerical simulations of cyclic storm behavior: Mesocyclogenesis and tornadogenesis. Ph.D. dissertation, University of Oklahoma, 217 pp. [Available from School of Meteorology, University of Oklahoma, 100 East Boyd, Suite 1310, Norman, OK 73019.]
- , K. K. Droegemeier, and R. P. Davies-Jones, 1999: A numerical simulation of cyclic mesocyclogenesis. *J. Atmos. Sci.*, **56**, 2045–2069.
- Alexander, C. R., and J. Wurman, 2005: The 30 May 1998 Spencer, South Dakota, storm. Part I: The evolution and environment of the tornadoes. *Mon. Wea. Rev.*, **133**, 72–96.
- Bluestein, H. B., and A. L. Pazmany, 2000: Observations of tornadoes and other convective phenomena with a mobile, 3-mm wavelength, Doppler radar: The spring 1999 field experiment. *Bull. Amer. Meteor. Soc.*, **81**, 2939–2951.
- , and S. G. Gaddy, 2001: Airborne pseudo-dual-Doppler analysis of a rear-inflow jet and deep convergence zone within a supercell. *Mon. Wea. Rev.*, **129**, 2270–2289.
- , C. C. Weiss, and A. L. Pazmany, 2003: Mobile Doppler radar observations of a tornado in a supercell near Bassett, Nebraska, on 5 June 1999. Part I: Tornadogenesis. *Mon. Wea. Rev.*, **131**, 2954–2967.
- , —, and —, 2004: The vertical structure of a tornado: High-resolution, W-band, Doppler radar observations near Happy, Texas, on 5 May 2002. *Mon. Wea. Rev.*, **132**, 2325–2337.
- Brandes, E. A., 1977: Gust front evolution and tornado genesis as viewed by Doppler radar. *J. Appl. Meteor.*, **16**, 333–338.
- , 1978: Mesocyclone evolution and tornadogenesis: Some observations. *Mon. Wea. Rev.*, **106**, 995–1011.
- , 1981: Finest structure of the Del City-Edmond tornadic mesocirculation. *Mon. Wea. Rev.*, **109**, 635–647.
- , 1984a: Relationships between radar-derived thermodynamic variables and tornadogenesis. *Mon. Wea. Rev.*, **112**, 1033–1052.
- , 1984b: Vertical vorticity generation and mesocyclone sustenance in tornadic thunderstorms: The observational evidence. *Mon. Wea. Rev.*, **112**, 2253–2269.
- , R. P. Davies-Jones, and B. C. Johnson, 1988: Streamwise vorticity effects on supercell morphology and persistence. *J. Atmos. Sci.*, **45**, 947–963.
- Carbone, R. E., M. J. Carpenter, and C. D. Burghart, 1985: Doppler radar sampling limitation in convective storms. *J. Atmos. Oceanic Technol.*, **2**, 357–361.

- Clark, T. J., F. I. Harris, and C. J. Mohr, 1980: Errors in wind fields derived from multiple Doppler radars: Random errors and temporal errors associated with advection and evolution. *J. Appl. Meteor.*, **19**, 1273–1284.
- Colby, F. P., Jr., 1984: Convective inhibition as a predictor of convection during AVE-SESAME II. *Mon. Wea. Rev.*, **112**, 2239–2252.
- Dowell, D. C., and H. B. Bluestein, 1997: The Arcadia, Oklahoma, storm of 17 May 1981: Analysis of a supercell during tornadogenesis. *Mon. Wea. Rev.*, **125**, 2562–2582.
- , and —, 2002a: The 8 June 1995 McLean, Texas, storm. Part I: Observations of cyclic tornadogenesis. *Mon. Wea. Rev.*, **130**, 2626–2648.
- , and —, 2002b: The 8 June 1995 McLean, Texas, storm. Part II: Cyclic tornado formation, maintenance, and dissipation. *Mon. Wea. Rev.*, **130**, 2649–2670.
- , Y. Richardson, and J. Wurman, 2002: Observations of the formation of low-level rotation: The 5 June 2001 Sumner County, Kansas, tornado. Preprints, *21st Conf. on Severe Local Storms*, San Antonio, TX, Amer. Meteor. Soc., CD-ROM, 12.3.
- , C. R. Alexander, J. M. Wurman, and L. J. Wicker, 2005: Centrifuging of hydrometeors and debris in tornadoes: Radar-reflectivity patterns and wind-measurement errors. *Mon. Wea. Rev.*, **133**, 1501–1524.
- Fujita, T. T., 1975: New evidence from the April 3–4, 1974 tornadoes. Preprints, *Ninth Conf. on Severe Local Storms*, Norman, OK, Amer. Meteor. Soc., 248–255.
- , and R. M. Wakimoto, 1982: Anticyclonic tornadoes in 1980 and 1981. Preprints, *12th Conf. on Severe Local Storms*, San Antonio, TX, Amer. Meteor. Soc., 213–216.
- Gal-Chen, T., 1982: Errors in fixed and moving frame of references: Applications for conventional and Doppler radar analysis. *J. Atmos. Sci.*, **39**, 2279–2300.
- Jensen, B., T. P. Marshall, M. A. Mabey, and E. N. Rasmussen, 1983: Storm scale structure of the Pampa storm. Preprints, *13th Conf. on Severe Local Storms*, Tulsa, OK, Amer. Meteor. Soc., 85–88.
- Klemp, J. B., and R. Rotunno, 1983: A study of the tornadic region within a supercell thunderstorm. *J. Atmos. Sci.*, **40**, 359–377.
- , R. B. Wilhelmson, and P. S. Ray, 1981: Observed and numerically simulated structure of a mature supercell thunderstorm. *J. Atmos. Sci.*, **38**, 1558–1580.
- Lee, W.-C., and J. Wurman, 2005: The diagnosed structure of the Mulhall tornado. *J. Atmos. Sci.*, **62**, 2373–2393.
- , B. J.-D. Jou, B.-L. Chang, and S.-M. Deng, 1999: Tropical cyclone kinematic structure retrieved from single ground-based Doppler radar. Part I: The ground-based VTD technique. *Mon. Wea. Rev.*, **127**, 2419–2439.
- Lemon, L. R., and C. A. Doswell, 1979: Severe thunderstorm evolution and mesocyclone structure as related to tornadogenesis. *Mon. Wea. Rev.*, **107**, 1184–1197.
- Ludlam, F. H., 1963: Severe local storms: A review. *Severe Local Storms, Meteor. Monogr.*, No. 27, Amer. Meteor. Soc., 1–30.
- Markowski, P. M., J. M. Straka, and E. N. Rasmussen, 2002: Direct surface thermodynamic observations within the rear-flank downdrafts of nontornadic and tornadic supercells. *Mon. Wea. Rev.*, **130**, 1692–1721.
- Neiman, P. J., F. M. Ralph, M. A. Shapiro, B. F. Smull, and D. Johnson, 1998: An observational study of fronts and frontal mergers over the continental United States. *Mon. Wea. Rev.*, **126**, 2521–2554.
- Rasmussen, E. N., and D. O. Blanchard, 1998: A baseline climatology of sounding-derived supercell and tornado forecast parameters. *Wea. Forecasting*, **13**, 1148–1164.
- , R. E. Peterson, J. E. Minor, and B. D. Campbell, 1982: Evolutionary characteristics and photogrammetric determination of windspeeds within the Tulia outbreak tornadoes 28 May 1980. Preprints, *12th Conf. on Severe Local Storms*, San Antonio, TX, Amer. Meteor. Soc., 301–304.
- Ray, P. S., R. J. Doviak, G. B. Walker, D. Sirmans, J. Carter, and B. Bumgarner, 1975: Dual-Doppler observation of a tornadic storm. *J. Appl. Meteor.*, **14**, 1521–1530.
- , C. L. Ziegler, and R. J. Serafin, 1980: Single- and multiple-Doppler radar observations of tornadic storms. *Mon. Wea. Rev.*, **108**, 1607–1625.
- , B. C. Johnson, K. W. Johnson, J. S. Bradberry, J. J. Stephens, K. K. Wagner, R. B. Wilhelmson, and J. B. Klemp, 1981: The morphology of several tornadic storms on 20 May 1977. *J. Atmos. Sci.*, **38**, 1643–1663.
- Richardson, Y., D. Dowell, and J. Wurman, 2001: High-resolution dual-Doppler analyses of two thunderstorms during the pre-tornadogenesis and mature tornado stages. Preprints, *30th Int. Conf. on Radar Meteorology*, Munich, Germany, Amer. Meteor. Soc.
- Romine, G., L. J. Wicker, and M. S. Gilmore, 2004: Analysis of simulated supercell tornadogenesis. Preprints, *22d Conf. on Severe Local Storms*, Hyannis, MA, Amer. Meteor. Soc., CD-ROM, 9.1.
- Sanders, F., and E. G. Hoffman, 2002: A climatology of surface baroclinic zones. *Wea. Forecasting*, **17**, 774–782.
- Stout, G. E., and F. A. Huff, 1953: Radar records Illinois tornadogenesis. *Bull. Amer. Meteor. Soc.*, **34**, 281–284.
- Tanamachi, R. L., H. B. Bluestein, S. S. Moore, and R. P. Madding, 2006: Infrared thermal imagery of cloud base in tornadic supercells. *J. Atmos. Oceanic Technol.*, **23**, 1445–1461.
- Trapp, R. J., 1999: Observations of nontornadic low-level mesocyclones and attendant tornadogenesis failure during VORTEX. *Mon. Wea. Rev.*, **127**, 1693–1705.
- , and R. Davies-Jones, 1997: Tornadogenesis with and without a dynamic pipe effect. *J. Atmos. Sci.*, **54**, 113–133.
- , E. D. Mitchell, G. A. Tipton, D. W. Effertz, A. I. Watson, D. L. Andra Jr., and M. A. Magsig, 1999: Descending and nondescending tornadic vortex signatures detected by WSR-88Ds. *Wea. Forecasting*, **14**, 625–639.
- Wakimoto, R. M., and C. Liu, 1998: The Garden City, Kansas, storm during VORTEX 95. Part II: The wall cloud and tornado. *Mon. Wea. Rev.*, **126**, 393–408.
- , and H. Cai, 2000: Analysis of a nontornadic storm during VORTEX 95. *Mon. Wea. Rev.*, **128**, 565–592.
- Weisman, M. L., and J. B. Klemp, 1982: The dependence of numerically simulated convective storms on the vertical wind shear and buoyancy. *Mon. Wea. Rev.*, **110**, 504–520.
- Wicker, L. J., and R. B. Wilhelmson, 1995: Simulation and analysis of tornado development and decay within a three-dimensional supercell thunderstorm. *J. Atmos. Sci.*, **52**, 2675–2703.
- , D. Dowell, Y. Richardson, and R. Wilhelmson, 2002: A large eddy simulation of a tornadic supercell: Comparison with observations. Preprints, *21st Conf. on Severe Local Storms*, San Antonio, TX, Amer. Meteor. Soc., 262–263.
- Wood, V. T., R. A. Brown, and D. Sirmans, 2001: Technique for improving detection of WSR-88D mesocyclone signatures by increasing angular sampling. *Wea. Forecasting*, **16**, 177–184.
- Wurman, J., 2001: The DOW mobile multiple-Doppler network.

- Preprints, *30th Int. Conf. on Radar Meteorology*, Munich, Germany, Amer. Meteor. Soc., CD-ROM, P3.3.
- , 2002: The multiple-vortex structure of a tornado. *Wea. Forecasting*, **17**, 473–504.
- , and S. Gill, 2000: Finescale radar observations of the Dimmitt, Texas (2 June 1995), tornado. *Mon. Wea. Rev.*, **128**, 2135–2164.
- , and M. Randall, 2001: An inexpensive, mobile, rapid-scan radar. Preprints, *30th Int. Conf. on Radar Meteorology*, Munich, Germany, Amer. Meteor. Soc., CD-ROM, P3.4.
- , and C. Alexander, 2004: Scales of motion in tornadoes, what radars cannot see, and what scale circulation is a tornado. Preprints, *22d Conf. on Severe Local Storms*, Hyannis, MA, Amer. Meteor. Soc., CD-ROM, P11.6.
- , and —, 2005: The 30 May 1998 Spencer, South Dakota, storm. Part II: Comparison of observed damage and radar-derived winds in the tornadoes. *Mon. Wea. Rev.*, **133**, 97–119.
- , J. M. Straka, and E. N. Rasmussen, 1996: Fine scale doppler radar observation of tornadoes. *Science*, **272**, 1774–1777.
- , —, —, M. Randall, and A. Zahrai, 1997: Design and deployment of a portable, pencil-beam, pulsed, 3-cm Doppler radar. *J. Atmos. Oceanic Technol.*, **14**, 1502–1512.
- , C. Alexander, P. Robinson, and Y. Richardson, 2007a: Low level winds in tornadoes and potential catastrophic tornado impacts in urban areas. *Bull. Amer. Meteor. Soc.*, **88**, 31–46.
- , Y. Richardson, C. Alexander, S. Weygandt, and P.-F. Zhang, 2007b: Dual-Doppler analysis of winds and vorticity budget terms near a tornado. *Mon. Wea. Rev.*, in press.
- Xue, M., 2004: Tornadogenesis within a simulated supercell storm. Preprints, *22d Conf. on Severe Local Storms*, Hyannis, MA, Amer. Meteor. Soc., CD-ROM, 9.6.